2022

Hypersonic non-equilibrium Computational Fluid Dynamics (CFD) analysis and effect of underbelly shape on a conceptual lifting body spaceplane

Barretto, O.G.

University of Plymouth

Hypersonic non-equilibrium Computational Fluid Dynamics (CFD) analysis and effect of underbelly shape on a conceptual lifting body spaceplane

Oliver George Barretto

Project Advisor: Adam Kyte, School of Engineering, Computing, and Mathematics, University of Plymouth, Drake Circus, Plymouth, PL4 8AA

Abstract

A methodology is developed to analyse the effect of underbelly shape on the force coefficients and adiabatic wall temperature acting on a lifting body spaceplane at 30° angle of attack and three Mach numbers (Ma=4, 10, 16) in air in the commercial Computational Fluid Dynamics (CFD) solver, Ansys Fluent. A general overview of hypersonic theory and phenomena is also presented.

The effect of hypersonic flow on gas dynamics is considered using a two-temperature non-equilibrium energy model and species transport simulation of reacting gases in Ansys Fluent. No third-party research of note is found validating the two-temperature Ansys Fluent non-equilibrium energy model due to only being recently implemented in 2021. Therefore, a focus of the investigation is validating the model against empirical results.

Validation of the numerical and physical models is performed by comparison against empirical wind tunnel investigations and flight data for simple shapes. Domain and mesh sensitivity studies are performed. CFD simulations of a blunt cone at Mach 6.77 matched a wind tunnel validation case by within 15-20% for lift and drag coefficients, and matched lift-to-drag ratio by 1-3%. CFD of ELECTRE test vehicle validation case matched flight data stagnation point heat flux to within 1%.

An attempt was made to determine the adiabatic wall temperature of a space vehicle re-entering from low Earth orbit, but poor agreement with theory was reached – suggestions are made to explain this, and recommendations for future work are discussed.

Keywords: Computational Fluid Dynamics, CFD, hypersonic, re-entry, non-equilibrium, Ansys Fluent, lifting body, validation, wind tunnel, aerodynamics

Introduction

A lifting body aircraft uses only its body to generate lift: i.e., it has no wings (except control surfaces). This generally reduces the glide ratio of the aircraft, but has advantages such as reduced mass, more effective use of internal volume and greater structural integrity. These advantages are crucial when applied to space vehicles – wings are dead mass when in a vacuum, and efficiency of volume is necessary to allow the maximum payload to be carried into space.

Historically, humans have travelled to and from space in blunt conic capsules. However, these are often at least partially non-reusable, experience high g-loads during re-entry and importantly have limited ability to aim at a specific landing site (Reed, 1997).

Another solution is a reusable, gliding re-entry vehicle using aerodynamic control surfaces and RCS thrusters to change direction and descent rate. Nominally, this results in the vehicle experiencing lower g-loads than a similar non-lifting body (Chapline & Hale, 2011), and importantly can reduce the peak heat experienced, at the expense of a greater total heat load on the body.

For hyper-velocity re-entry, it is not practical to fully test designs physically – ground testing capability is usually limited to matching only 1-2 of the relevant flow characteristics, e.g. Mach number, Reynolds number or aerothermal effects (Eberhardt, 2009). Therefore, the application of CFD to this case is invaluable for evaluating key aerodynamic design decisions.

Project motivation

Lifting body spacecraft have applications for LEO operations but could potentially also be used in future for lunar re-entry or extraplanetary atmospheric entry e.g., Mars or Titan. These situations generally involve speeds and energies almost an order of magnitude greater than that that occur during LEO re-entry ($E_k = \frac{1}{2}mv^2$), and so it is important to first consider a methodology for evaluating and predicting performance for this more 'simple' case in CFD, so that additional effects and flow characteristics can be added e.g. gas ionisation at interplanetary re-entry velocities (Gallais, 2007).

Additionally, no significant literature is found dedicated to the effect of longitudinal underbelly radius on thermal and aerodynamic performance of a lifting body.

Aims

Three convex underbelly shapes plus one experimental, waverider-inspired (Ding, et al., 2017) concave shape will be considered for this investigation. The aim is to reduce surface heat temperature and thermal loads on the vehicle, while maximising L/D during the high supersonic to hypervelocity flight regime.

Objectives

1. Develop methodology to analyse hypersonic flow in a commercial CFD solver that can be applied generally to future investigations – ensuring accuracy by validating against empirical data and experiments.
2. Validate the capability of a commercial CFD solver to model non-equilibrium and reacting fluid flow.

3. Analyse the effect of changing underbelly shape on maximising L/D ratio and minimising thermal loads on a generic lifting body test shape (hereafter referred to as the Briefly Imagined Lifting Body Orbiter – or **BILBO**, for short).

Throughout this report, the Space Shuttle will be used as an approximate comparison due to the wealth of data that exists for it and its similar application of interest – the only reason it hasn't been used as a validation case is that its geometry is complex and prone to discrepancies.

Literature review

Only a brief overview of the relevant topics from existing literature in the context of CFD is presented here, with references given for further reading – it would be impossible to fully explain all relevant aspects of hypersonic aerothermodynamics in ~1600 words.

Computational fluid dynamics (CFD)

CFD is the application of computing power to generate an approximate numerical solution for a defined flow field.

The finite-volume method is used in many commercial CFD solvers to first discretise the flow domain into many smaller cells (Versteeg & Malalasekera, 1995) - known as meshing - over which the governing Navier-Stokes partial differential equations (PDEs) can be approximately solved iteratively. For supersonic compressible flow, density changes must also be considered, resulting in the 3D unsteady compressible form of the Navier-Stokes equations (Anderson, 1992):

Lifting body physics

$$\frac{\partial u}{\partial x} + \frac{\partial v}{\partial y} + \frac{\partial w}{\partial z} = 0$$

$$\rho \left[\frac{\partial u}{\partial t} + \frac{\partial u}{\partial x} u + \frac{\partial u}{\partial y} v + \frac{\partial u}{\partial z} w \right] = -\frac{\partial p}{\partial x} + \mu \left(\frac{\partial^2 u}{\partial x^2} + \frac{\partial^2 u}{\partial y^2} + \frac{\partial^2 u}{\partial z^2} \right) + \rho g_x$$

$$\rho \left[\frac{\partial v}{\partial t} + \frac{\partial v}{\partial x} u + \frac{\partial v}{\partial y} v + \frac{\partial v}{\partial z} w \right] = -\frac{\partial p}{\partial y} + \mu \left(\frac{\partial^2 v}{\partial x^2} + \frac{\partial^2 v}{\partial y^2} + \frac{\partial^2 v}{\partial z^2} \right) + \rho g_y$$

$$\rho \left[\frac{\partial w}{\partial t} + \frac{\partial w}{\partial x} u + \frac{\partial w}{\partial y} v + \frac{\partial w}{\partial z} w \right] = -\frac{\partial p}{\partial z} + \mu \left(\frac{\partial^2 w}{\partial x^2} + \frac{\partial^2 w}{\partial y^2} + \frac{\partial^2 w}{\partial z^2} \right) + \rho g_z$$

Figure 1: 3D unsteady compressible form of the Navier-Stokes governing equations

Lifting bodies employ two main mechanisms for lift generation. First is the concept of Newtonian flow-turning lift, wherein the vehicle has a surface angled to the oncoming flow (AoA) which 'deflects' the air particles down and turns the flow (Messiter, 1963). Newton's third law states that this will produce an equal but opposite reaction force

on the body surface, producing lift. Importantly, this effect does not just occur on the underbelly, but the upper surface can also turn the flow, depending on its angle of attack.

Secondarily, 'Bernoulli' pressure lift occurs when the body at an angle of attack generates a higher-pressure region below the vehicle due to compression of the gas. This generates a net positive force over the body, producing lift.

Hypersonic aerodynamics

Mach number is the ratio of the speed of a body to the local speed of sound c in the fluid. It is dependent on temperature T, gas constant R, molecular mass M and ratio of specific heats γ in an ideal gas:

$$c = \sqrt{\frac{\gamma RT}{M}}$$

Equation 1: Speed of sound in a fluid

When the Mach number of a body Ma_∞ exceeds 1, a fluid discontinuity known as a shockwave is formed because no information can travel through the flow faster than the body. Pressure, temperature and density increase by an order of magnitude across this shock (Ferri, 1949). Shockwaves are considered adiabatic because no energy is added (isenthalpic) and no heating necessarily occurs by the shock (NASA Glenn Research Center, 2007). Adiabatic compression of the gas in front of a supersonic body shockwave results in a temperature and pressure rise as described by the ideal gas law.

$$pV = m\dot{R}T$$

Equation 2: Ideal gas law

Hypersonic flight is experienced when Ma_∞ becomes so great that specific flow characteristics become a significant design consideration – often identified as being when $Ma_\infty > 5$, but this is only an approximate rule of thumb – these effects can variably occur at $\sim 3 < Ma < \sim 12$, depending on geometry and other considerations. Hypersonic flow is qualified by the following physical effects:

1. High temperature flow and severe aerodynamic heating
2. Thick boundary layers that scale with $\frac{Ma^2}{\sqrt{Re_x}}$
3. Thin shock layers
4. Entropy layers

Re-entry vehicles usually have blunted forms to reduce aerodynamic heating due to the following correlation (Anderson, 1984), where q is heat flux and r_n is nose radius:

$$q \propto \frac{1}{\sqrt{r_n}}$$

Equation 3: Relationship between nose radius and heat flux

When a blunt supersonic vehicle travels through a gas, a detached 'bow shock' is formed because the required rotation of the fluid exceeds the maximum rotational

angle required for the shock to remain obliquely attached to the surface (Ben-Dor, 2007).

The prediction and calculation of oblique (angled to surface) and normal (perpendicular to surface) shocks is possible analytically for flat surfaces and sharp cones/wedges (see (Anderson, 1982) for full details). However, for blunt bodies such as blunted cones or complex geometries at angles of attack, no such analytical solution exists – therefore, specific numerical techniques have been developed to solve the 'blunt body problem'. The time-marching technique is utilised significantly in modern CFD codes and involves assuming an initial value for a discretised flowfield, before 'marching' the solution forward in time over a given time step (Δt) (Anderson, 1984).

Lift and drag coefficient (C_L and C_D respectively) are non-dimensional characteristics of a shape defined by the following equations:

$$C_L = \frac{2F_L}{\rho u_\infty^2 A}$$

Equation 4: Lift coefficient

$$C_D = \frac{F_d}{\rho A \frac{u_{\infty^2}}{2}}$$

Equation 5: Drag coefficient

where F_d=drag force, F_L=lift force, u_∞=freestream flow velocity and A=reference area of the body. The lift and drag forces are calculated by integrating the pressure over the surface with respect to area in the intended direction vectors.

Total drag force is the sum of lift-induced and parasitic drag, which is composed of skin friction and form pressure drag (Clancy, 1975). For re-entry bodies at an angle of attack with significant flow separation, form drag is a far greater contributor to overall drag than skin friction (Anderson, 1984).

It is more useful to characterise a body using the non-dimensional coefficients rather than absolute force values for comparison irrespective of shape or size (Clancy, 1975). Maximising L/D ratio logically improves vehicle glide ratio, increasing cross-range capability especially in the high atmosphere where groundspeeds are significantly higher.

(Anderson, 1982) states that an infinite flat plate is theoretically the most efficient hypersonic lifting surface possible. From this theory, it is expected that the lifting body shape with a flat underbelly will produce the highest L/D ratio. However, a key purpose of this work is to identify what effect this has on wall temperature with relation to L/D ratio, in comparison to other body shapes.

The stagnation point of a body in a flow refers to a point on its surface where the fluid velocity reduces to zero (Clancy, 1975). Therefore, all the kinetic energy of the

fast-moving fluid is transferred to internal heat energy, so it experiences the highest surface temperature, pressure and density on the body. (Anderson, 1982) states that the stagnation point usually occurs at the nose of a hypersonic vehicle, but a secondary stagnation point can occur at other large surface discontinuities e.g., control surfaces.

Significant literature is available on quantifying stagnation point aerodynamic heating correlations for a wide range of flows. The Sutton-Graves correlation equation (NASA TFAWS, 2012) relates stagnation heat flux to nose radius, density and velocity using an atmospheric constant k (k=1.7415x10^{-4} for Earth):

$$q_{stag} = k \left(\frac{\rho}{r_n}\right)^{\frac{1}{2}} * V^3$$

Equation 6: Sutton-Graves stagnation point heat flux correlation

Adiabatic compression in the hypersonic shock layer can heat the gas to several thousands of degrees (Candler, 2007), which convectively dissipates the heat into the vehicle's wake. However, only a small percentage of heat should reach the surface of the body, due to massive temperature gradients in the viscous boundary layer. The heat that reaches the body is called the 'adiabatic wall temperature' (or 'recovery temperature').

State-of-the-art
CFD has reached sufficient maturity (Papadopoulos, et al., 1999) to inform practical design decisions for development of hypersonic gliding weapons, high-speed airliners, and TPS design. However, these applications typically use specifically developed codes to consider phenomena of relevance (Maicke & Majdalani, 2010). An approach to simulating hypersonic flow in a general-purpose commercial solver is therefore still desirable and of note.

Hypervelocity effects on gas properties

Non-equilibrium flow
A gas is in thermal non-equilibrium when its energy cannot be characterised by a single temperature. Instead, four energies – translational, rotational, vibrational and electronic – must be used (Candler, 2007). When a hypersonic flow meets a body, the huge kinetic energy of the individual particles is converted to random motion before collisions in the bow shock layer transfer energy to the other three states. This affects the internal energy and chemical composition of the gas and must be modelled in CFD with a two-temperature (translational-rotational and vibration-electronic) gas model (see (Anderson, 1989) for a more in-depth breakdown).

Gas dissociation
The most basic models of fluid flow assume a thermally and calorically perfect gas, where γ is constant and Equation 2 is obeyed. However, multi-molecular gases, such as air, experience dissociation due to high flow temperature experienced during hypersonic flight. At temperatures between 2000K and 4000K, O_2 dissociates, while

N₂ begins at 4000K (Balu & Raj, 2012). These reactions change the thermal properties of the gas and mean that γ cannot be assumed to be constant. Gas dissociation is also key to removal of some of the heat from the surface of the re-entry body (Candler, 2007).

The Park 5-species transport model (Park, et al., 2001) numerically simulates chemical dissociation effects using a finite-rate reaction, while discounting ionisation. c_p and γ are calculated as a 9-coefficient polynomial function, while k is derived from the Eucken formula (Eckert, 1971):

$$K = \mu \left(c_p + \frac{10.4}{M} \right)$$

Equation 7: Eucken thermal conductivity formula (Ubbelohde, 1946)

Rarefied flows
Knudsen number is a non-dimensional number defined as the ratio of the molecular mean free path length to a characteristic length scale. It quantifies rarefaction (significantly low fluid density) of a gas and can be related to Mach and Reynolds number by the following equation:

$$Kn = \frac{Ma}{Re} \sqrt{\frac{\gamma \pi}{2}}$$

Equation 8: Knudsen number

This assumes a constant γ, ρ and μ but is a sufficient approximation to determine whether continuum mechanics is valid (treating the fluid is a continuous mass rather than individual particles) when Kn<0.1, (Beskok, et al., 2005)). For all simulations undertaken in this project, the Fluent built-in Knudsen number calculator was used to verify this assumption for the considered flowfields.

For the sake of future work, methods that can be used for these more rarefied conditions are described in (Josyula & Burt, 2011) but will not expanded on here.

Critical review of sources
Where possible, peer-reviewed papers (AIAA, Cambridge Core etc) and textbooks were used to source information. The series of textbooks by John D. Anderson on aerodynamics are referenced heavily, due to their wide acceptance as the defining sources on the subjects. For some methodology choices (e.g., solution control values) no particular reference is found for application to hypersonic flows. Therefore, a compilation of research and approximation from sources such as online forums is used to suggest a correct value.

METHODOLOGY

Problem clarification

For the final BILBO simulations, only a steady state simulation is considered – time-dependent unsteady effects will be modelled with a turbulence model. In the immediate reference frame, the vehicle velocity is assumed to be constant. The effect of gravity is also assumed to be negligible. Three Mach number simulations will be considered (Ma=4, 10 and 16), to analyse a range of re-entry flight regimes over the range where the Space Shuttle experienced peak heating (

Figure).
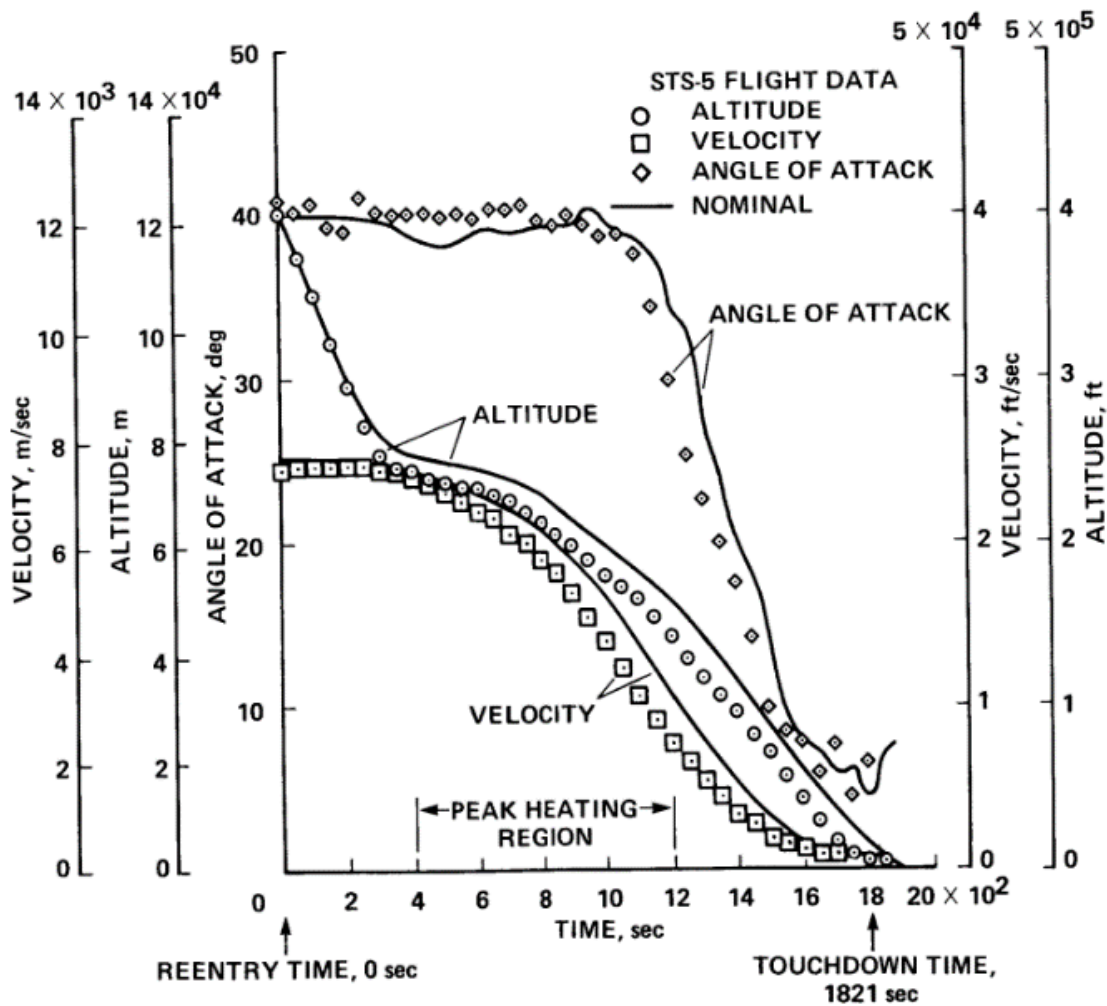
Figure 2: STS-5 re-entry trajectory from nasa.org specifically Ko *et al.* (1986)

Approximate trajectory and operating conditions (angle of attack (AoA or α) and altitude) are estimated from Space Shuttle trajectory (Figure 2), with atmospheric properties from US Standard Atmosphere (NOAA, 1976). Only one value of each will be considered so that the variable of underbelly shape is isolated and can be evaluated.

Table 1: Freestream conditions of interest

AoA /°	Altitude /km	p /Pa	ρ /kgm^{-3}	T /K
30	50	79.78	1.03×10^{-3}	270.65

Three values for underbelly radius will be analysed – flat (infinite radius), 12m and 6m. Additionally, an experimental waverider-inspired 12m concave configuration will be tested. The hypothesis expected from theory (Cockrell Jr, et al., 1996) is that this shape will improve L/D ratio by maximising compression lift from a bow shock induced high-pressure 'cushion' of air beneath its underbelly (Ding, et al., 2017). The shape of the bow shock wave is largely invariant to detailed surface shape (Wan & Liu, 2017).

The outputs of the final lifting body simulations will be the following:

1. C_L and C_D
2. Lift-to-drag (L/D) ratio
3. Maximum wall-adjacent temperature of underbelly
4. Contours
    a. Underbelly surface temperature
    b. Flow temperature, pressure and velocity

CFD solver consideration
Several CFD solvers were considered, both commercial and open-source. Ansys Fluent (hereafter referred to as just 'Fluent') was chosen due its density-based solver (preferable for compressible supersonic flows (ANSYS, 2009), robust user interface and species transport models (to simulate gas dissociation). Additionally, recent versions of the software (2021R2, released in December 2021) have integrated a non-equilibrium, two-temperature energy model to better simulate hypersonic flows. Validating the effect of both this and the species transport model will be a focus of the investigation, due to the minimal literature found validating particularly the two-temperature model due to its recent implementation.

Validation cases
Quantifying error for CFD is somewhat difficult (NASA Glenn Research Center, 2002) – therefore, validation and verification against empirical test results is crucial to ensure credibility of results and reduce human error in implementing models and correct boundary conditions.

Table 2: Summary of validation cases

No.	Description	Purpose	Mach number	Non-equilibrium + reacting?	Validation case
1	3D pitched blunt cone at α=0°, 27°, 55°, 60°, 40°	Validation of bow shock shape and force coefficients of a 3D case at angles of attack. Domain/mesh dependency study to determine the effect of wake and skin turbulence modelling on results	6.77	No	(Neal Jr., 1963)
2	ELECTRE test vehicle flight data at α=2° in non-equilibrium, reacting air	Verification of thermal prediction and non-equilibrium and species transport model in Fluent	13	Yes	(Muylaert, et al., 1992)

The two validation cases serve to validate the following:

1. Blunt body flow and shock prediction.
2. Accurate hypersonic lift and drag coefficients.
3. Non-equilibrium energy model and species transport reacting gas simulation.

Validation case 1 will compare CFD against a 1963 hypersonic wind tunnel experiment of a blunted cone (only II configuration due to similar length-to-base ratio as BILBO) at Ma=6.77 (Neal Jr., 1963). Six values of α will be simulated – 0°, 10°, 20°, 27°, 40° and 55° - as they are AoAs that are both approximately within the range of the angles of attack that will be analysed for the final case and have the Schlieren shock images provided for 0° and 27° in the literature for comparison.

The DDS flow conditions used will be a Ma=4, α=30° case. This is because it is expected from normal shock theory (Anderson, 1982) that the nose bow shock distance will increase as Mach number reduces, and so the maximum extents of the final simulation can be found.The bow shock shape simulation must be validated to ensure that the pressure and density flowfield is accurate for determination of force coefficients (Miller, 1998).

The issue of limited experimental data arises for validating non-equilibrium flow models. Hypersonic wind tunnel tests are usually either unable to simulate high enthalpy flow effects such as flow dissociation (Eberhardt, 2009), or use monatomic working gases such as nitrogen, hydrogen and helium (which does not account for 5-species reactions).

Therefore, validation case 2 will compare CFD against real ELECTRE test vehicle heat flux data - a 1m long, blunted cone geometry launched on a sub-orbital trajectory in 1971 (Muylaert, et al., 1992).

Mesh generation
To accelerate the geometry and mesh creation, a single mesh was developed for use with all the angle of attack variations of each simulation.The domains used for both the blunted cone validation cases and the final lifting body simulations will be a 45° blunted cone to reduce inlet discontinuities.

Shock capturing strategy
To ensure good convergence and results for supersonic and hypersonic CFD simulations, it is of utmost importance to consider the alignment of the mesh cells such that they match the shape of the expected shock as closely as possible (Anderson, 1982).However, for all the blunt body CFD simulations it is unknown what exact shape the shock will take, or the bow shock distance. Therefore, an approximately parabolic shock-aligned mesh (expected from literature) will be used. Dynamic mesh adaption could be used to refine the mesh across regions of maximum density gradient to increase mesh resolution and capture the bow shock more accurately. This method will be attempted and verified by comparing the relevant output variables.

The effectiveness of using the standard Ansys Meshing software to construct structured grids is limited, particularly for complex, organic shapes as will eventually be required for this investigation. Therefore, the block-dominated meshing functionality in Ansys Spaceclaim is used to manually generate approximately shock aligned meshes for both the validation and final cases. This also allows the use of hexahedron mesh elements, accelerating and improving solution quality (Bhaskaran & Collins, 2012).Mesh density should be highest in the approximately expected stagnation region of the body to capture the high temperature, pressure and density gradients in this area (Papadopoulos, et al., 1999).

Domain dependency study
Hypersonic vehicles can have wakes extending many times their body length (Lykoudis, 1964). This is unfeasible and unnecessary to fully simulate (mesh size would also logically increase, requiring more computational resource and extended simulation time), particularly for this investigation, where the relevant output variables are primarily affected by forebody and shock interaction. This assumption must be verified using a domain dependency study (DDS), to find the domain size at which not capturing the turbulent wake no longer affects the output variables.

A domain independency will be performed for validation case 2 (3D pitched blunt cone) due to its similar base-to-length ratio as the BILBO shapes. The process involves first using an intentional large domain size to establish a baseline result, before using a much smaller domain to observe if the results change, and further modifying the domain to reduce this change (Δ).

A key characteristic of supersonic flows is that no information can be transferred downstream of the shock, so it is expected that the domain distance in front of the body is not required to be as significant as the other dimensions.

Mesh dependency study
Boundary layer and wall resolution must have sufficient quality to capture thermal and viscous gradients next to the body surface. Once a domain dependency study has been performed, the effect of mesh resolution must also be quantified by using different mesh resolutions and methods to observe changes in the output variables.

Boundary layer development
The dimensionless quantity y^+ is used to quantify boundary layer resolution for CFD simulations. From (Yu, et al., 2021), it is suggested that a value of $y^+ = 1$ with a cell growth rate of 1.1 should be used for hypersonic boundary layers.

The process to calculate a first layer height for a targeted y^+ is based on flat plate boundary layer theory from (White, 1979) and results in the following equation (using constant freestream density). To account for unknown, changing viscosity due to flow temperature, μ will be taken to be 1% of the SSL air viscosity (1.789×10^{-5} Pas):

$$\Delta s = \frac{y^+ \mu}{\rho \sqrt{\dfrac{\left(\left(\dfrac{0.026}{Re_x^{\frac{1}{7}}}\right) * \rho * u_\infty^2\right)}{2}} }$$

Equation 9: First mesh cell spacing

where Re_x is Reynolds number based on length:

$$Re_x = \frac{\rho u_\infty L}{\mu}$$

Equation 10: Reynolds number based on length

Turbulence model
That hypersonic flow is intrinsically unsteady (Anderson, 1984) means that modelling of time dependent turbulence effects is of paramount importance. The flow is assumed to be completely turbulent (Marvin & Coakley, 1989) so no transition model will be used.

Transient Large Eddy Simulation (LES), Detached Eddy Simulation (DES) and Direct Numerical Simulation (DNS) were all considered to simulate large vortices in the turbulent hypersonic wake – however, (Roy & Blottner, 2006) states that the effectiveness of these in hypersonic flows is still the subject of research and development, as well as being unnecessarily computationally intensive and not required for this investigation. Therefore, a Reynolds-Averaged-Navier-Stokes (RANS) model is used instead (Spalart & Allmaras, 1992).

The single-equation (modified turbulent viscosity) Spalart-Allmaras model was developed specifically for aerospace applications. As such, it is considered numerically robust for a wide range of flow regimes (Tong, 2013). (Sinha, 2010) suggests that it offers similar accuracy to flight data for heat flux.

Heat transfer

Convective heating
High mesh resolution near the surface is imperative to resolve the thermal gradients present in the boundary layer for accurate prediction of surface thermal characteristics. To consider the adiabatic wall temperature, the CFD wall must be set to a zero-heat flux boundary condition, with a specified temperature. Conjugate heat transfer through the body will not be considered, as the material is not known a priori.

Radiative heating
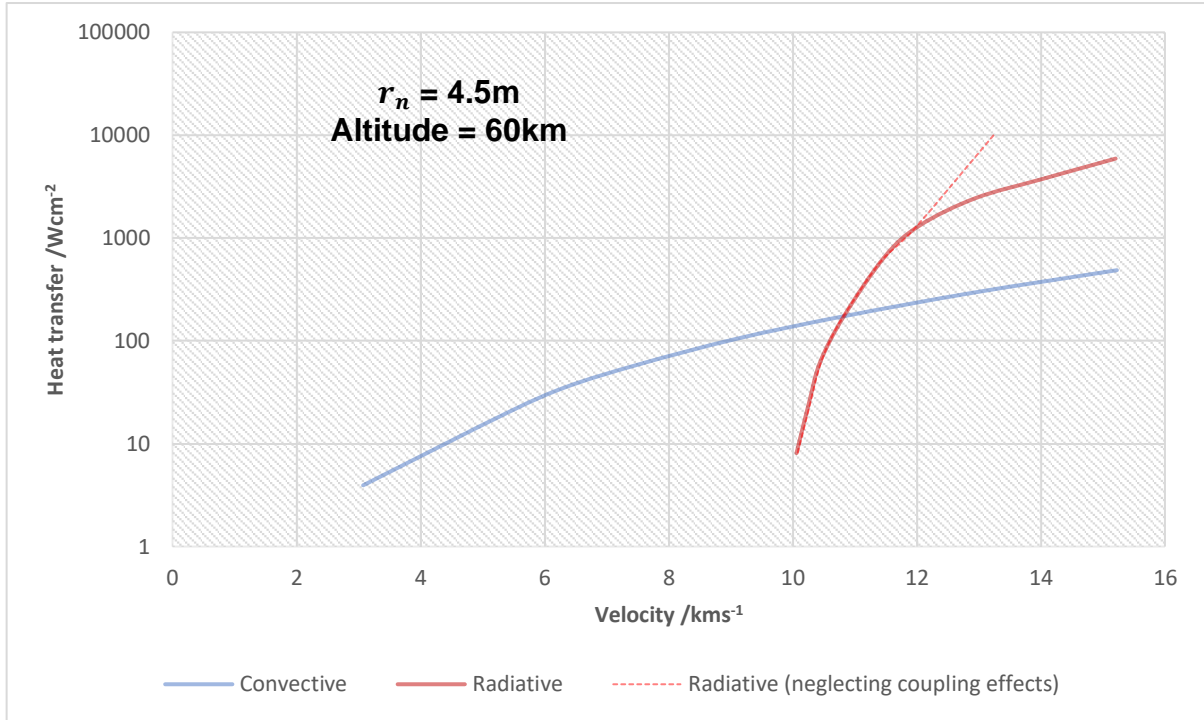
Figure 3: Relative importance of radiative and convective heat transfer for the specified body adapted from (Anderson, 1989)

Figure shows that for the flow velocity of interest (~1800-5300ms^{-1}), radiative heat transfer should not be as significant a consideration as convective. For this reason, it will be neglected for the CFD simulations (retrospectively, this was potentially a serious oversimplification).

Fluid properties

Density
The 'ideal-gas' option for density in Fluent is chosen, so that compressible flow, viscous heating and total energy can be considered by the solver.

Viscosity
Due to the huge temperature changes experienced during hypersonic flight, gas viscosity cannot be assumed to be close to constant. The three-coefficient Sutherland viscosity law (Equation 11, where μ_0, T_0 and S are Sutherland constants) is used to represent viscosity as a function of temperature. The coefficients and

plotted curve for air viscosity against temperature are taken from the default Fluent material library:

$$\mu = \mu_0 \left(\frac{T}{T_0}\right)^{\frac{3}{2}} \frac{T_0 + S}{T + S}$$

Equation 11: Three-coefficient Sutherland viscosity law

Implementation of high temperature gas effects
The two-temperature energy and Park 5-species transport model in Fluent are activated to approximate the effects of non-equilibrium flow.

Settings/boundary conditions

Inlet
The inlet was set as a 'pressure-far-field' boundary condition, with a temperature and gauge pressure of the ambient atmospheric conditions for each case.

Outlet
The conditions at the domain outlet are not inherently known – however, it is expected that beyond a certain domain size, the flow will not tend to significantly re-enter the domain in the reference frame of the vehicle (Wood, et al., 2003). Therefore, the outlet boundary condition will be set to 'Prevent Reverse Flow' in Fluent, such that outlet conditions are not required to be specified.

Other considerations
Due to the symmetric nature of all the 3D simulations in this project, only half-domains with a symmetry plane will be used to reduce the mesh size, computational cost and simulation time.

Importance of initialisation
Due to the iterative nature of CFD, the initial 'guess' used for the solution has a significant effect on the speed and stability of convergence. FAS Multigrid (FMG) initialisation will be used to provide a starting point for the solution – it iteratively generates a coarser mesh, from which it calculates an inviscid, first-order approximate solution for the flowfield and species transport, if present (ANSYS, 2009).

Computational method
The implicit solver was used in Fluent to reduce simulation time associated with explicit solution of stretched meshes in high Reynolds number viscous hypersonic flow (Longo, 2004). This also means that choice of Courant number (C) is not as important, although solution stability is affected when C>5 (Caminha, 2019). Initial test simulations determined that C=0.7 offered a good compromise between solution stability and computational time.

After FMG initialisation, second order numerics are used for Flow, Turbulent Viscosity and Two-Temperature model to improve solution accuracy.

Numerical simulation of 3D shock waves using compressible upwind inviscid Euler equations can lead to a solution instability known as the carbuncle phenomenon, resulting in poor shock capturing and evaluation of continuity parameters. Its full explanation is complex and beyond the scope of this report (see (Pandolfi &

D'Ambrosio, 1999) for further details), but to resolve it, the Advection Upstream Splitting Method (AUSM) is used in Fluent to add an artificial dissipation term to 'smear' expansion shocks and remove the solver's reliance on normal and transverse shock elements (Jain, 2007). The proprietary 'High-Speed Numerics' and 'Convergence Acceleration for Stretched Meshes' were activated in Fluent. Double precision numerics were used to reduce floating point and truncation errors (Mou, et al., 2017).

Time step Δt
For explicit computation, the Courant-Friedrichs-Lewy (CFL) stability criterion states that the time step (Δt) can be described by the following (Anderson, 1982):

$$\Delta t \leq \frac{minimum\ cell\ characteristic\ length\ l_c}{freestream\ velocity\ u_\infty} * K_t$$

where $K_t < 1$. For implicit formulation, this criterion can be relaxed to reduce simulation time, such that $\Delta t = \frac{l}{u_\infty}$.

Convergence criteria
For most CFD simulations, a residuals convergence criterion of 10^{-6} is deemed suitable for an accurate solution (Kuron, 2015). However, for more complex and high velocity flowfields such as hypersonic, between 10^{-3} and 10^{-4} for continuity and 10^{-5} for energy is suggested by (Shevkar, 2016). Arguably of greater importance (Kuron, 2015) is to ensure that the relevant output variables (force coefficients, thermal characteristics) converge to a steady state. Therefore, a steady solution convergence criterion of 10^{-3} for all report definitions is introduced.

Design of lifting body shape
A highly simplified geometry for a proposed delta planform lifting body spaceplane (BILBO) was modelled in Solidworks such that r_u was parametrically modifiable.

Conceptually, the shape was sized and designed to hypothetically reflect capabilities of existing spaceplanes such as the SNC Dream Chaser.

Table 3: Summary of BILBO shape dimensions

Further design would be required to verify and validate this shape beyond the aerodynamic analysis performed in this report, but it serves the purpose of isolating the intended shape variables. Projected frontal area for each body was found using Solidworks and halved for use as the reference area in Fluent (due to half domain).

Body shape name	r_u	A /m²	r_n	L	S	H
BILBO-1	6m convex	42.4				
BILBO-2	12m convex	42.3	4m	14m	8m	3.7m
BILBO-3	Flat	42.2				
BILBO-4	12m concave	42.2				
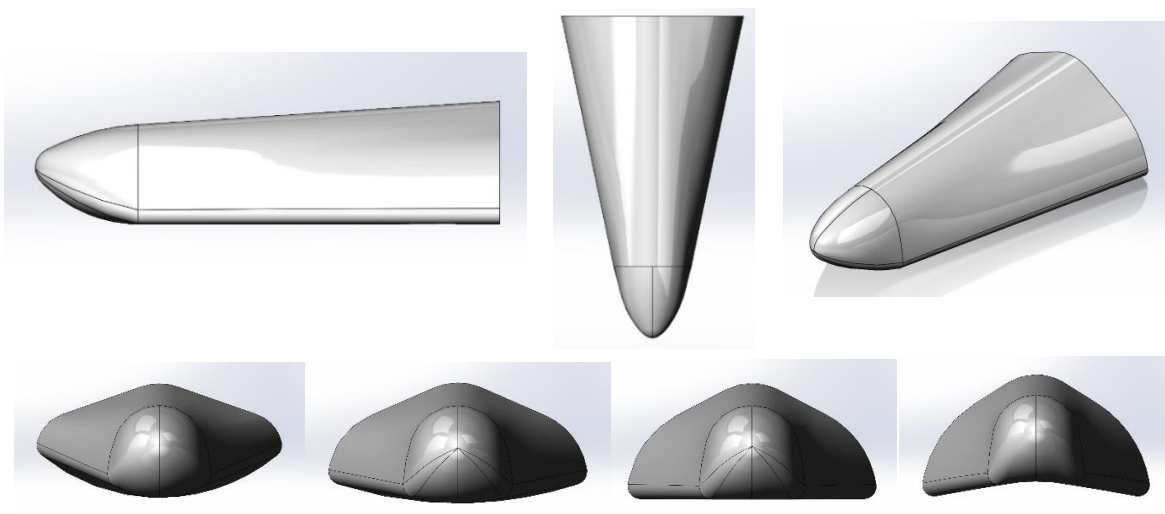
Figure 4: Orthographic views of the BILBO vehicle – BILBO-1, BILBO-2, BILBO-3 and BILBO-4 shown respectively

Methodology summary
Not considered

- RCS thruster plume impingement
- Radiative heating
- Stability and control characteristics
- Conjugate heat transfer
- Transient effects

The simulations were performed on University of Plymouth computers with the hardware and solver settings shown in

Table .

Table 4: Computational hardware used

Ansys version	2021R2
CPU	Intel i7-9700 8-core @3GHz
GPU	NVIDIA Quadro K2200
RAM	32 GB
Number of CPU solver processes	4
Number of GPU solver processes	0

Validation case simulations and results

Simulation matrix

Validation case 1 – 3D pitched blunt cone at Mach 6.77 in air

Table 5: Validation case CFD simulation matrix

Validation	Geometry	Purpose	Type	Mach	Angle of attack	Non-eq?
1	Pitched blunt cone	Domain dependency 1	3D	4	30	No
2	Pitched blunt cone	Domain dependency 2	3D	4	30	No
3	Pitched blunt cone	Mesh dependency 1	3D	6.77	27	No
4	Pitched blunt cone	Mesh dependency 2	3D	6.77	27	No
5	Pitched blunt cone	Mesh dependency 3	3D	6.77	27	No
6	Pitched blunt cone	Mesh dependency 4	3D	6.77	27	No
7	Pitched blunt cone	Mesh dependency 5	3D	6.77	27	No
8	Pitched blunt cone	Mesh dependency 6	3D	6.77	27	No
9	Pitched blunt cone	Validation 1	3D	6.77	0	No
10	Pitched blunt cone	Validation 2	3D	6.77	10	No
11	Pitched blunt cone	Validation 3	3D	6.77	20	No
12	Pitched blunt cone	Validation 4	3D	6.77	40	No
13	Pitched blunt cone	Validation 5	3D	6.77	27	No
14	Pitched blunt cone	Validation 6	3D	6.77	55	No
15	ELECTRE	Validation 1	3D	13	2	No
16	ELECTRE	Validation 2	3D	13	2	Yes

Mesh generation
No attempt was made to size the mesh accurately to achieve a particular y^+ for the DDS, since it is only concerned with the change in results due to domain size. Therefore, the DDS results should not be considered realistically accurate. Mesh size was controlled for the MDS.

Results and discussion

Domain dependency study (DDS)
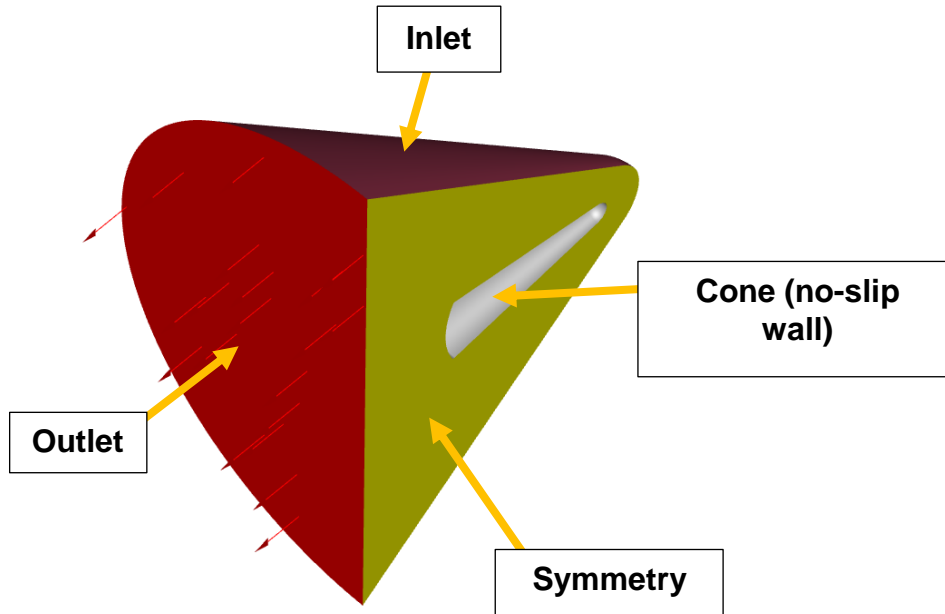
Figure 5: Domain boundaries
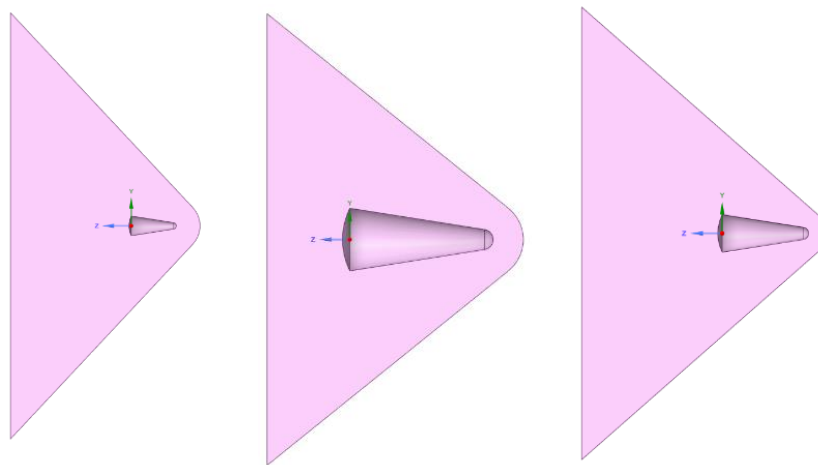
Figure 1: Domains 1, 2 and 3, respectively

Table 6: Freestream conditions for domain dependency study

Ma_∞	p_∞ /Pa	u_∞ /ms^{-1}	T_∞ /K	T_w /K	ρ_∞ /kgm^{-3}	α /°	L /m
4	101325	1898.4	560.9	300	1.26	30	0.137

The same mesh settings were used for all domain tests – with a minimum orthogonal quality of 0.124 and maximum skewness of 0.876.

Table 7: Domain dependency study results summary

Domain	Downstream	Upstream	Radius	Mesh elements	Lift coefficient	% change from baseline result	Drag coefficient	% change from baseline result	Surface-weighted average wall-adjacent temperature /K	% change from baseline result
1	0.5L	2.5L	4.5L	387000	0.9267	0.00%	0.6008	0.00%	2191.84	0.00%
2	0.2L	0.5L	1.5L	387000	0.9299	0.35%	0.5773	-3.91%	1940.94	-11.45%
3	0.2L	1.2L	2.5L	384400	0.9235	-0.34%	0.6003	-0.07%	2187.40	-0.20%

The criteria used to assess domain and mesh independence are C_L, C_D and surface-weighted average wall-adjacent temperature (T_{s_ave}) to assess how the surface temperature changed over the body using a single value.
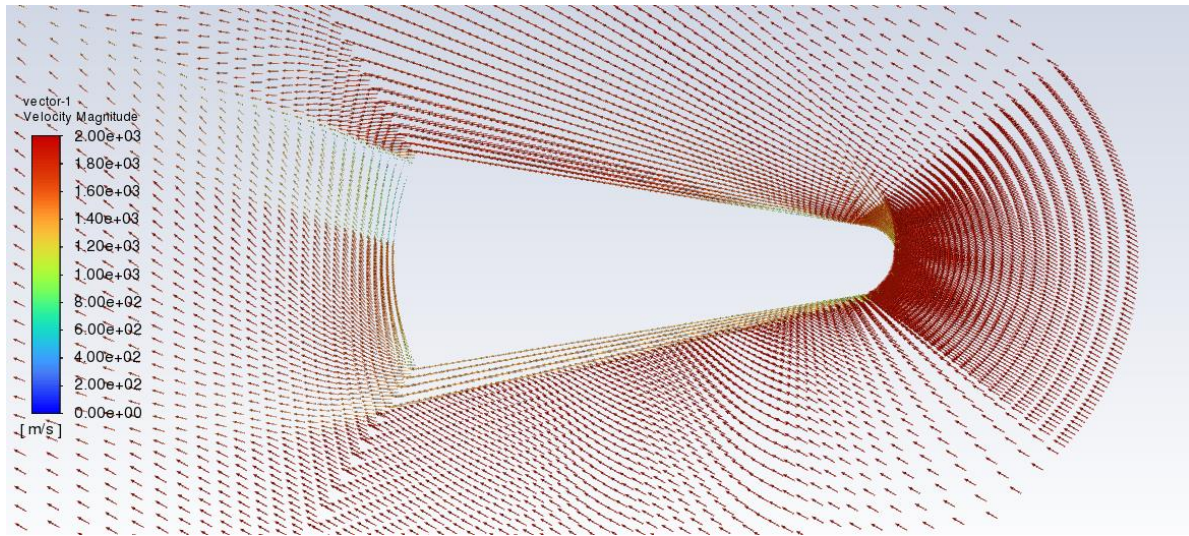
Figure 7: Velocity vector plot for the largest Domain 1

The results of the DDS showed a relatively domain-invariant C_l, but the values for C_d and T_{s_ave} changed noticeably for the smallest domain. The reason for this is apparent in Figure 8 – the upstream constriction of the domain causes the recirculating turbulent wake to produce a lower velocity, higher-pressure wake region, affecting the overall flowfield around the body.
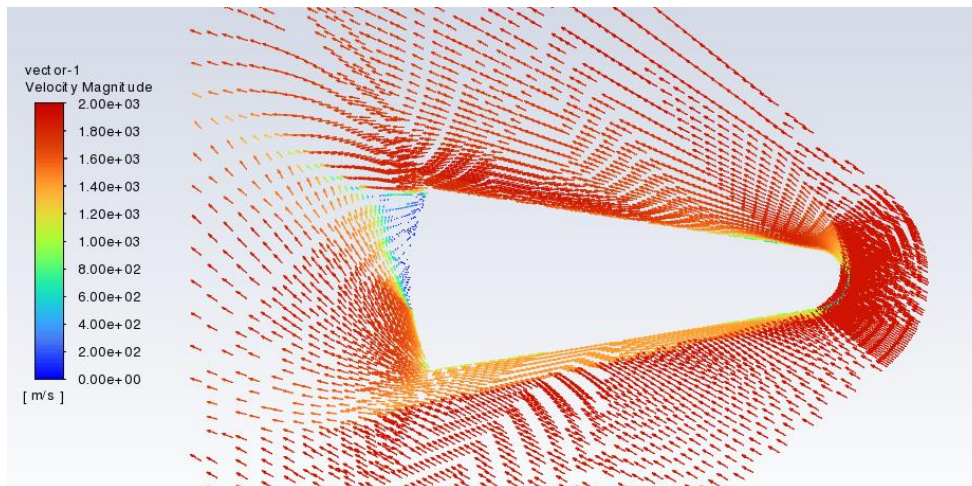
Figure 8: Velocity vector plot for the smallest Domain 2

Subsequently, the domain was changed to that shown in Figure 9, which reduced Δ to only -0.20%.
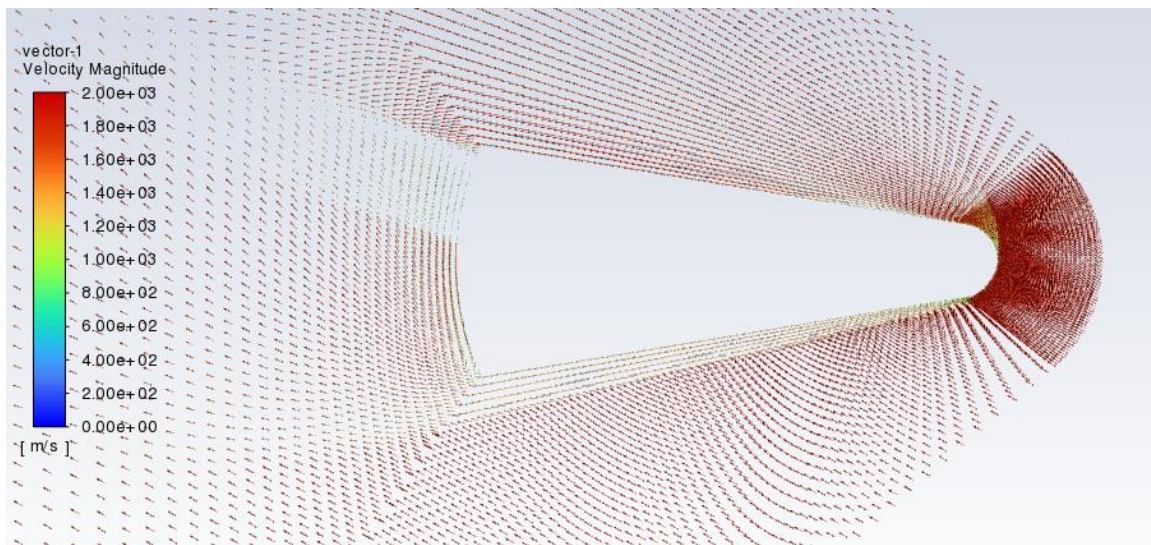
Figure 9: Velocity vector plot for the final Domain 3

Mesh dependency study (MDS)
The rest of the simulations for this validation used the freestream conditions from the empirical results and $\alpha=27°$

Table 8: Freestream conditions for validation case 1 MDS and comparison

Ma_∞	p_∞ /Pa	u_∞ /ms^{-1}	T_∞ /K	T_w /K	ρ_∞ /kgm^{-3}	α /°	L /m
6.77	18800	3213.0	560.9	300	1.16x10^{-1}	27	0.137

Table 9: Mesh dependency study table

Mesh	Circumferential elements	Radial elements	Axial elements	Total mesh elements N (post-adaption)	y$^+$	Shock mesh adaption	Lift coefficient	% change from baseline result	Drag coefficient	% change from baseline result	L/D ratio	% change from baseline result	Surface-weighted average wall-adjacent temperature /K	% change from baseline result	N^(1/3)	Simulation time
1	160	80	160	6236000	1	No	0.4673	0.00%	0.577	0.00%	0.81	0.00%	1633.4	0.00%	184.1	12 hrs 42 mins
2	120	60	120	2524000	1	No	0.4666	-0.15%	0.571	-1.08%	0.82	0.94%	1653.8	1.25%	136.2	4 hrs 27 mins
3	80	40	80	768800	1	No	0.4664	-0.19%	0.574	-0.46%	0.81	0.26%	1648.4	0.92%	91.6	2 hrs 11 mins
4	80	40	80	1165000	1	Yes	0.4650	-0.50%	0.573	-0.72%	0.81	0.23%	1646.6	0.81%	105.2	2 hrs 52 mins
5	40	20	40	327000	1	Yes	0.4614	-1.26%	0.580	0.48%	0.80	-1.73%	1678.8	2.78%	68.9	1 hr 23 mins
6	80	40	80	814250	0.25	No	0.4668	-0.10%	0.574	-0.56%	0.81	0.47%	1629.8	-0.22%	93.4	2 hrs 42 mins
7	80	40	80	734550	5	No	0.4666	-0.15%	0.571	-1.08%	0.82	0.94%	1721.6	5.40%	90.2	1 hr 57 mins
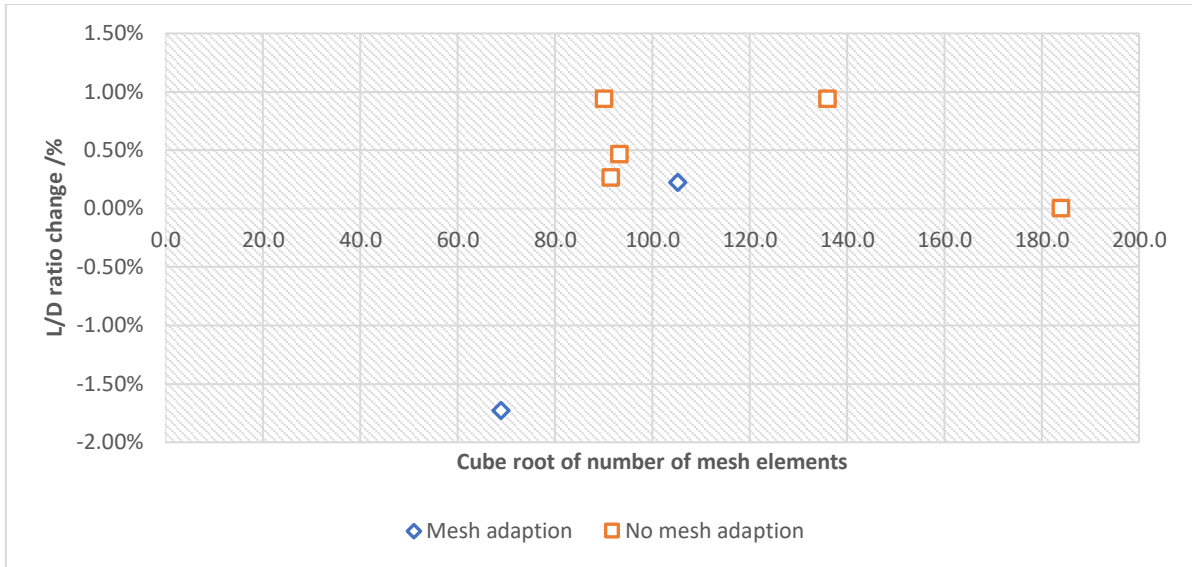
**Figure 10:** Effect of mesh resolution on L/D ratio prediction
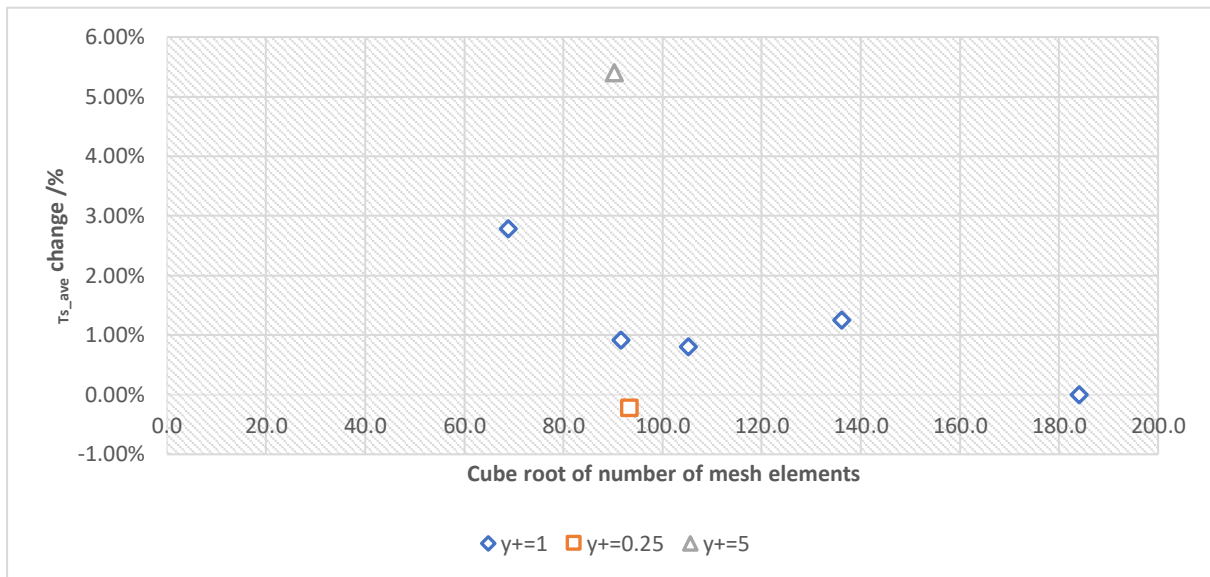
Figure 11: Effect of mesh resolution on T_{s_ave} prediction
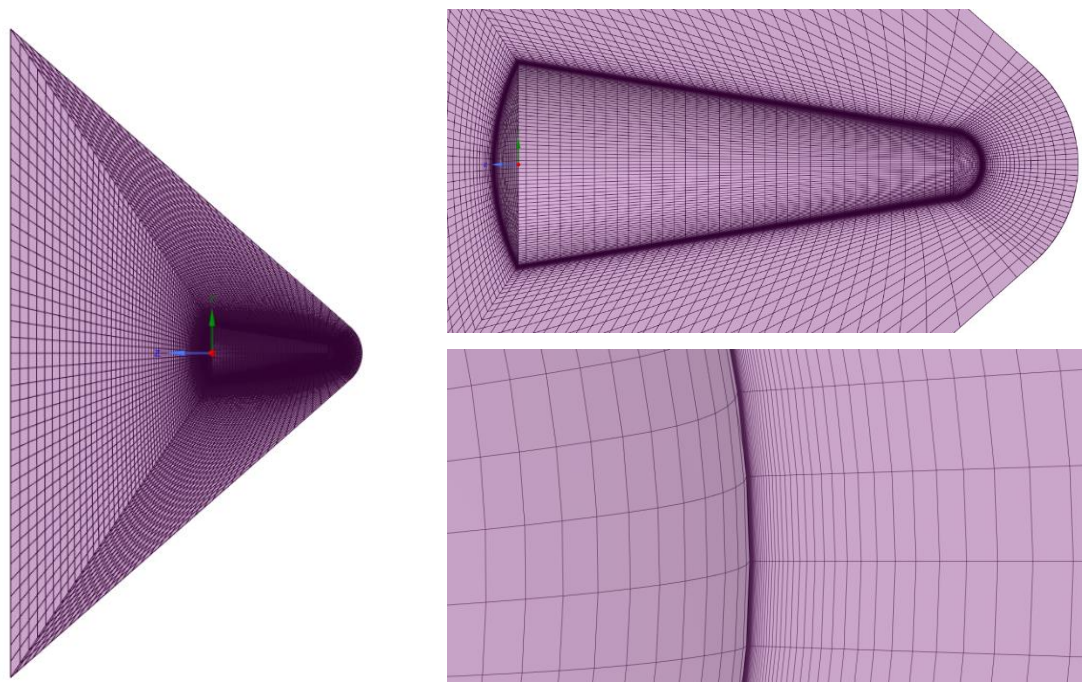
Figure 12: 'Mesh 2' computational grid, showing high resolution at expected stagnation point – number of grid elements halved for clarity on overall picture

'Mesh 1' was taken to be the 'baseline' result due to the assumption that flow characteristics would be more accurately calculated on the most refined grid – however, due to its large number of elements (6,236,000) the simulation took significantly longer to converge (12 hrs 42 mins).
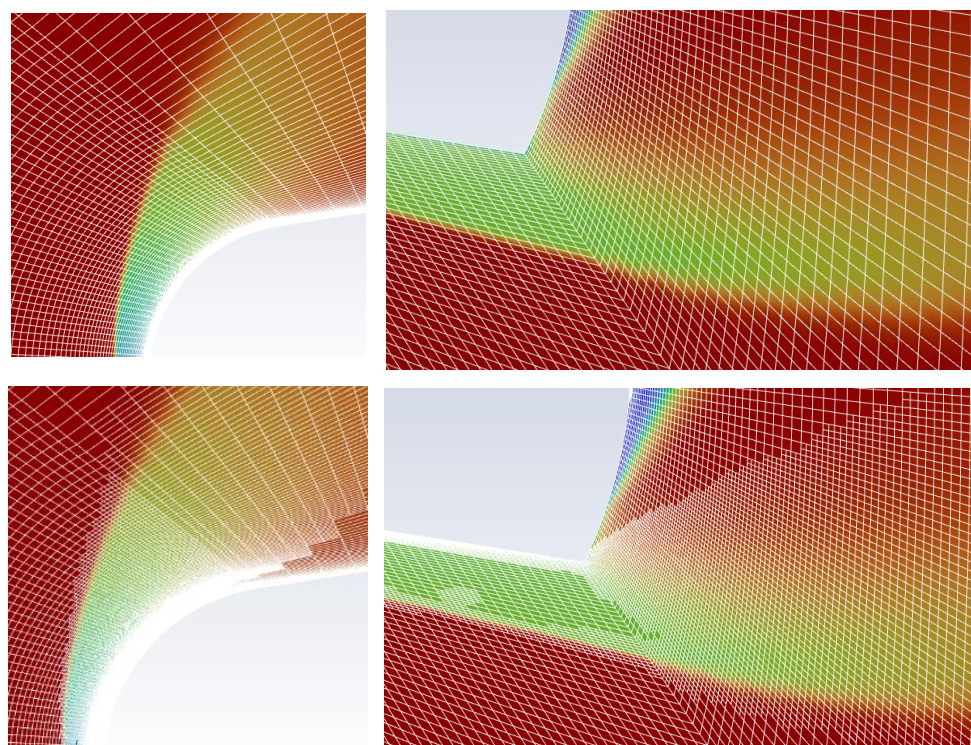
Figure 13: The effect of activating automatic shock-capturing density gradient mesh adaption on the leading and trailing edges of the blunt cone

Both overall mesh resolution and y^+ value were compared (summarised in Table 9). Immediately it is apparent that surface-weighted average wall-adjacent temperature T_{s_ave} changes significantly by correctly sizing the mesh for a y^+ of 1 (compared to DDS results).

The results demonstrate that the force coefficients are relatively mesh-invariant, with a change of only 0.94% between the most and least refined, non-adapted mesh L/D ratio (Figure). This matches expectations, as the majority of blunt body drag is due to pressure drag, meaning that boundary layer mesh control is less important.

However, T_{s_ave} was much more sensitive to y^+ - expected due to high flow property gradients in hypersonic boundary layers (Anderson, 1989) - a value of $y^+=5$ yielded Δ=5.40%, while $y^+=0.25$ yielded Δ=-0.22%.

The effect of using mesh adaption was found to be minimal on either force coefficients or temperatures (only 0.81% L/D change for Mesh 4), while increasing the element count and simulation time. Therefore, it will not be utilised in the final simulations.

Thus, the mesh quality used in Mesh 2 will be used in the final lifting body simulations, using an edge bias sizing to achieve the intended y^+ at the larger simulation scale.
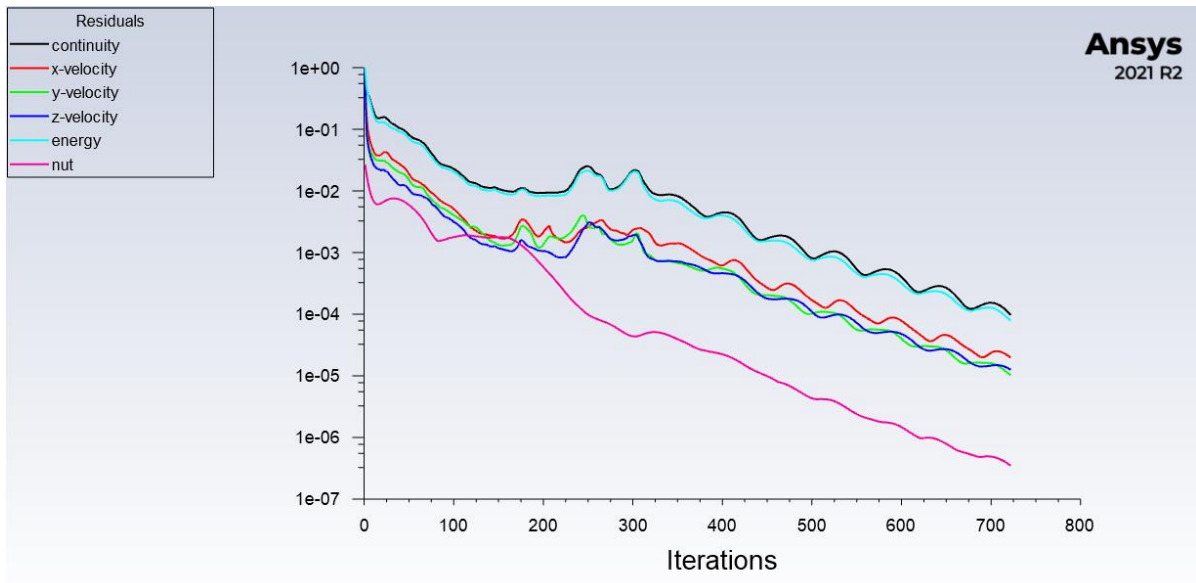
Figure 14: A typical residuals graph for these simulations, showing convergence to 10^{-4} – note, many simulations took far more than ~700 iterations to converge

Shock shape

The Schlieren shock images overlaid onto density plots in Figure 15 and Figure 16 show accurate recreation of the shock shape in CFD, validating that the compressible flow simulation predicts flow density and pressures correctly for blunt bodies at angles of attack.
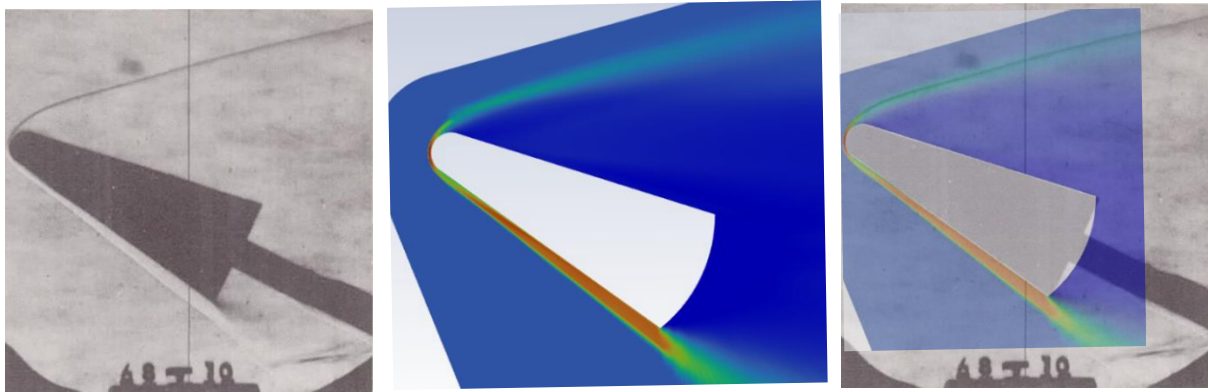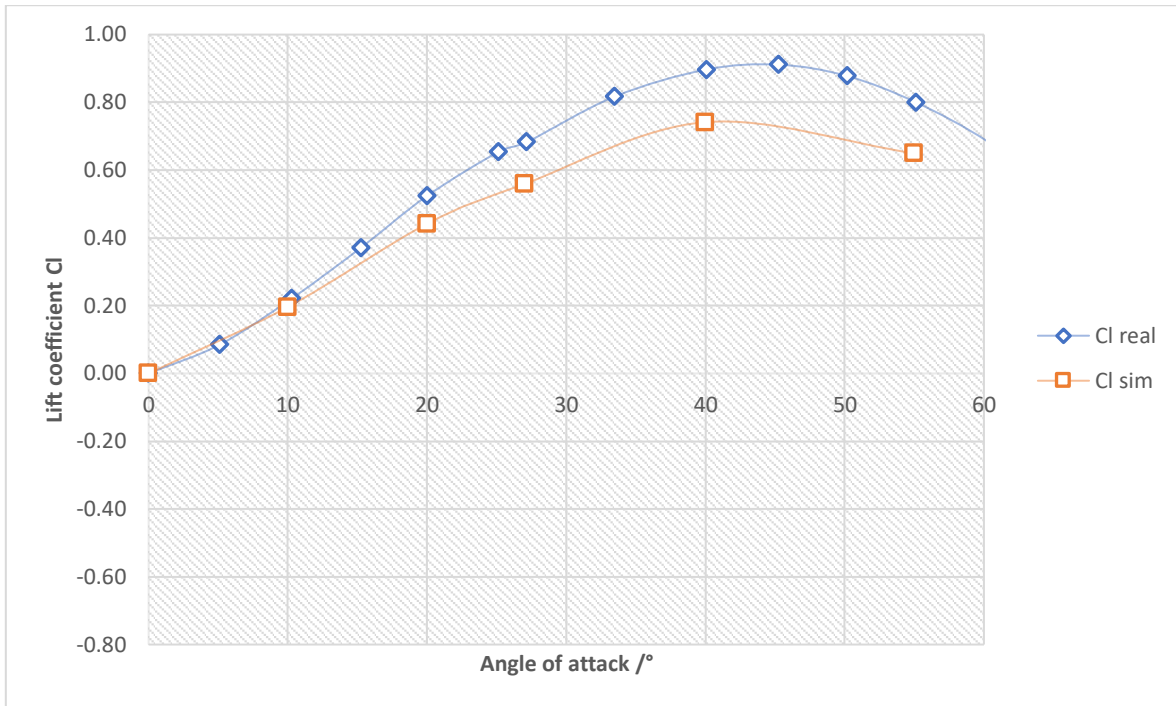
Figure 15: Schlieren, CFD density plot and overlaid images of cone at α=27° at Ma=6.77 (Base images from Nasa.org, Neal, 1963)
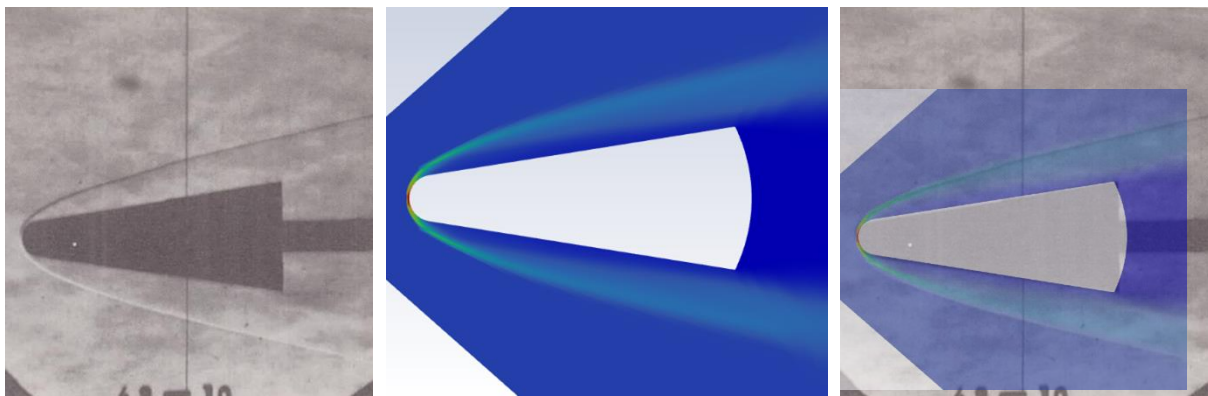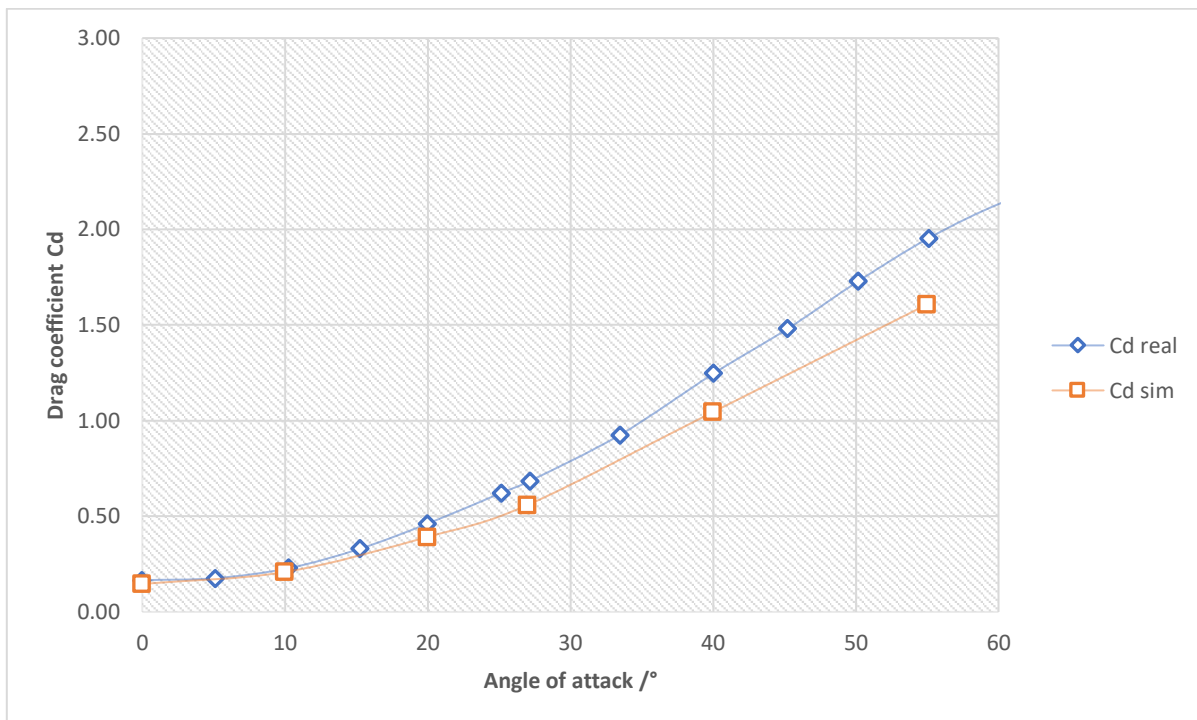
Figure 162: Schlieren, CFD density plots and overlaid images of cone at α=0° at Ma=6.77 **(Base images from Nasa.org, Neal, 1963)**

Force coefficients

Figure 17: Lift coefficient plotted against angle of attack for 3D blunt cone validation

Figure 18: Drag coefficient plotted against angle of attack for 3D blunt cone validation

Figure 19 shows excellent agreement for L/D ratio with empirical results, with a maximum deviation of only 3%. However, a systematic underprediction of C_L and C_D of between 15 and 20 percent is observed. This could be due to the CFD not

simulating the effect of no-slip wind tunnel walls (causing an unexpected velocity gradient and flow rebounding) or the empirical results not correcting for wind tunnel blockage correction (wherein the flow is constricted by the shape of the test body, and thus accelerates, potentially causing an overprediction of drag coefficient). This should be kept in mind for the final BILBO simulations, although it should not affect the shape assessment using L/D ratio.
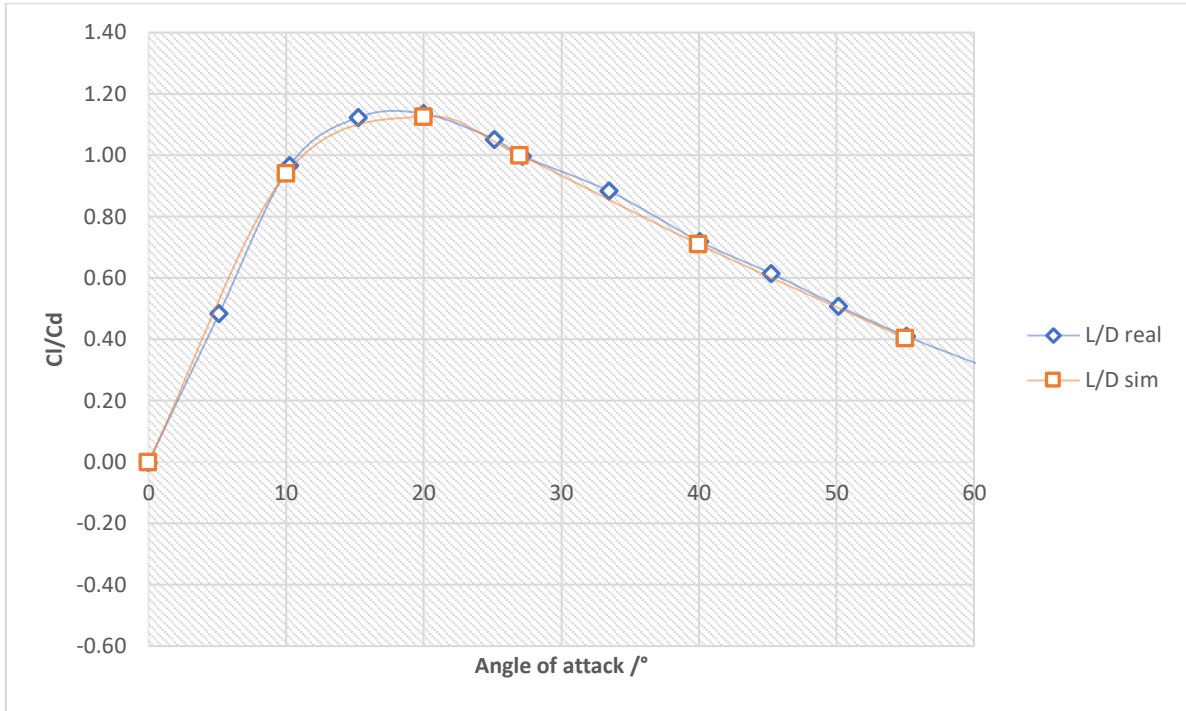
Figure 19: L/D ratio plotted against angle of attack for 3D blunt cone validation

Validation case 2 – ELECTRE flight test at Mach 13, α=2° in non-equilibrium, reacting air

Simulation settings

The same domain extents found in the validation case 1 DDS were used for the ELECTRE mesh. A high-resolution mesh with a y^+ of 1 was generated (80 elements circumferentially and axially, 40 radially with edge bias) for a total mesh element number of 837,460.

An isothermal wall temperature of 343K was used to match the measured flight data (Muylaert, et al., 1992). Freestream conditions were as per Table 10.

Table 10: Freestream conditions for ELECTRE validation case

Ma_∞	p_∞ /Pa	u_∞ /ms^{-1}	T_∞ /K	T_w /K	ρ_∞ /kgm^{-3}	α /°
13	53	4230	265	343	6.944x10^{-4}	2

Results and discussion

Heat flux

The ELECTRE flight only recorded heat flux using thermocouples at discrete points on its surface – therefore, accuracy of heat flux comparison between CFD and empirical will logically validate that the flow temperature prediction is accurate, as heat flux is a function of temperature change.
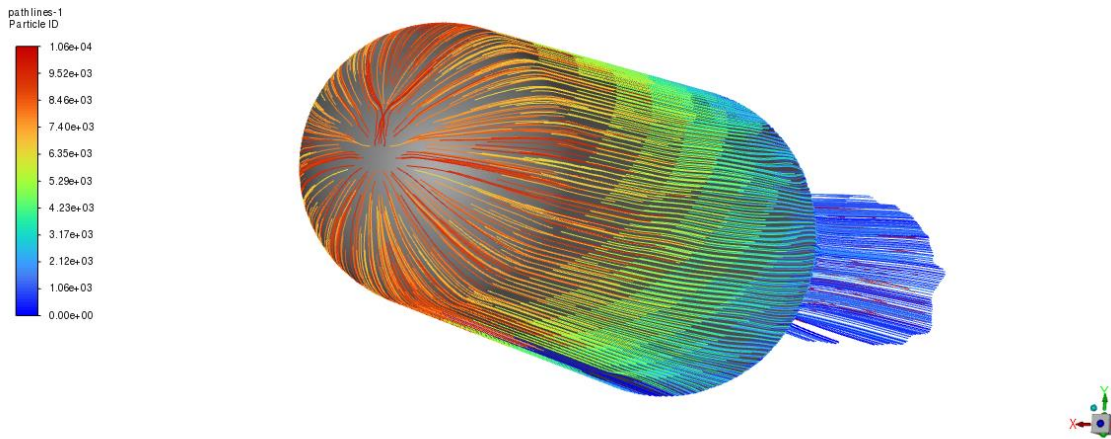

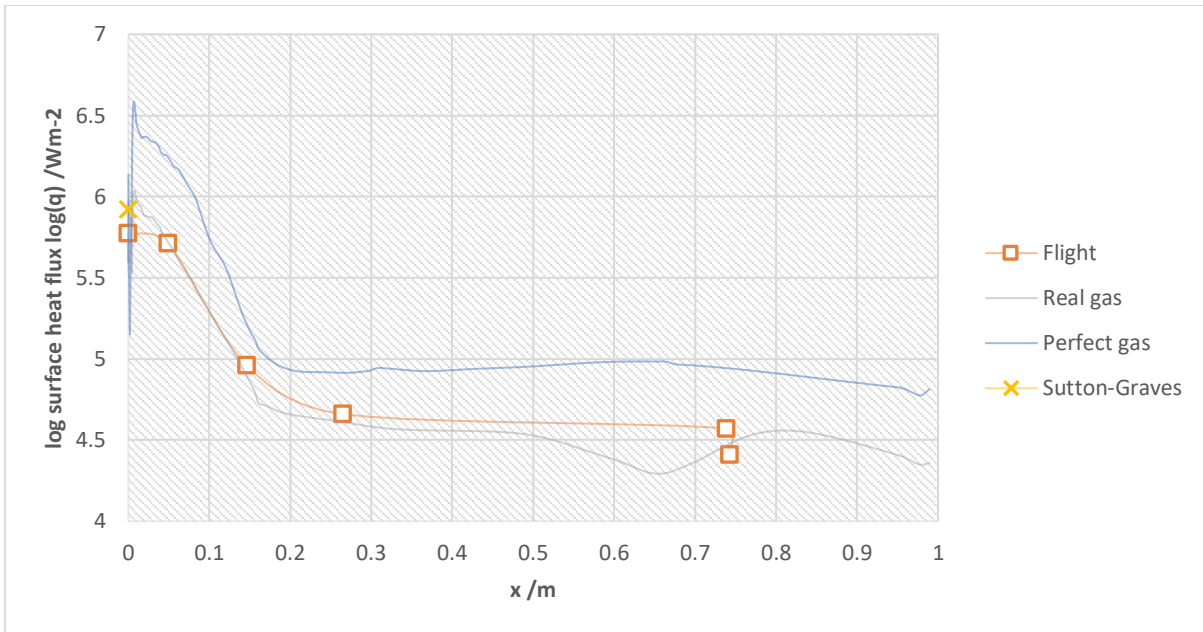**Figure 20:** Pathlines of particle ID for ELECTRE validation case

Figure 21: Log graph of surface heat flux against x-distance from stagnation point

The results for heat flux along the lower stagnation line of the body show remarkable similarity with the flight data over most of the body surface. Particularly, the effect of using the Fluent two-temperature and species transport is demonstrated to predict

surface heat flux more accurately when compared to the perfect gas model, suggesting that the inbuilt Fluent models are highly effective in analysing heat transfer and thermal prediction for hypersonic vehicles.

Additionally, the Sutton-Graves correlation (Equation 6) was used to find the theoretical stagnation point heating and plotted on the graph. This result also agreed very well with both the CFD and the flight data. A minor deviation in the results is shown for both the non-equilibrium and perfect gas results at approximately x=0.65m (Figure 22).
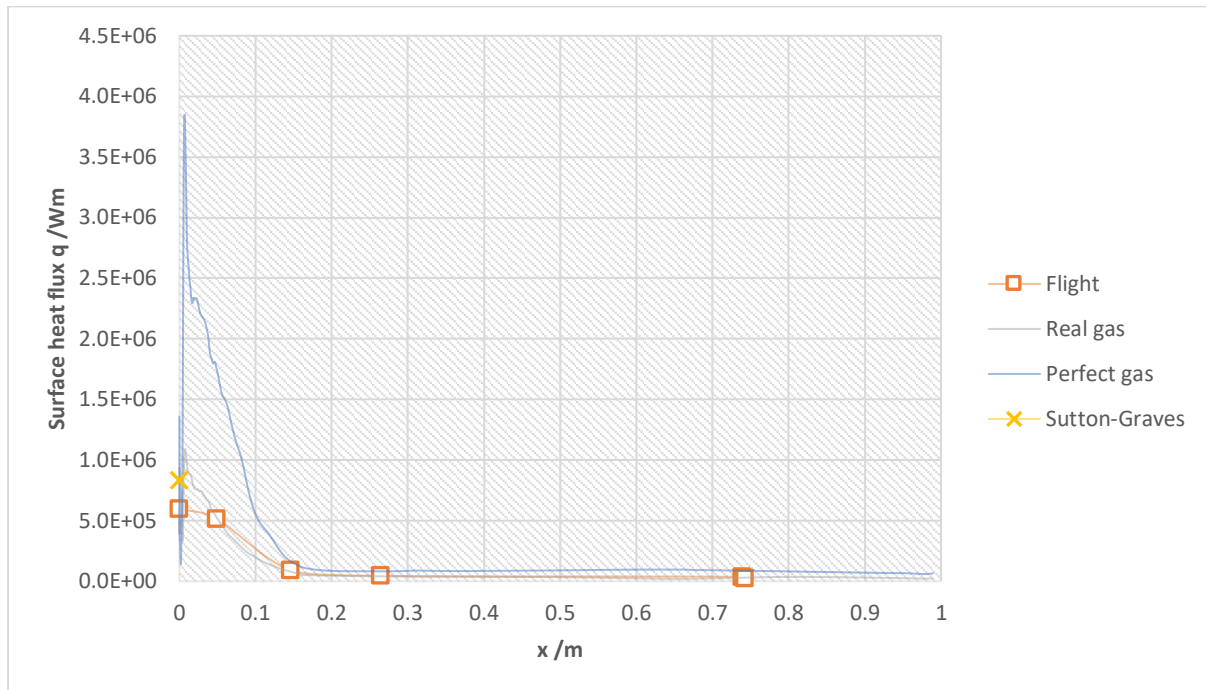
Figure 22: Surface heat flux against x-distance from stagnation point

This suggests flow separation, further reinforced by the velocity vectors shown in Figure 23. The resolution of the flight data is not sufficient to capture this region of the body due to the discrete placement of the thermocouples on the body, and the flow recovers to approximately the expected value at x=~0.74m, with only a discrepancy of 0.23%.
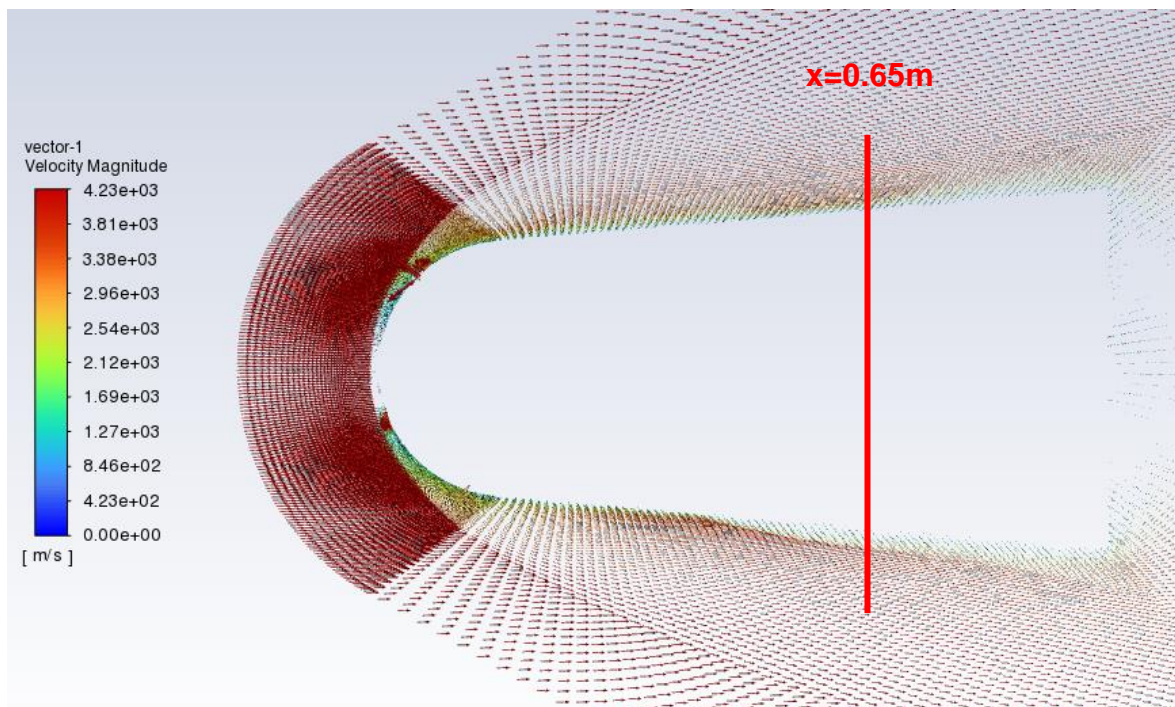
Figure 23: Velocity magnitude vectors of ELECTRE validation case showing flow separation

# Final lifting body simulations and results

Simulation matrix

Table 11: BILBO simulations matrix

Simulation	Underbelly radius	Angle of attack	Mach number
1	BILBO-1 - 6m	30	4
2	BILBO-1 - 6m	30	10
3	BILBO-1 - 6m	30	16
7	BILBO-2 - 12m	30	4
8	BILBO-2 - 12m	30	10
9	BILBO-2 - 12m	30	16
13	BILBO-3 - Flat	30	4
14	BILBO-3 - Flat	30	10
15	BILBO-3 - Flat	30	16
19	BILBO-4 - 12m concave	30	4
20	BILBO-4 - 12m concave	30	10
21	BILBO-4 - 12m concave	30	16

Simulation settings

The first wall cell size was calculated to be 1.17x10^{-6} m to achieve a y^+ of 1 at Ma=16 – this allowed the same mesh to be used for all Mach numbers.

Due to complex geometry at the nose and base, the blocks for these sections are swept quadrilateral elements rather than hexahedron radially mapped (Figure 24).
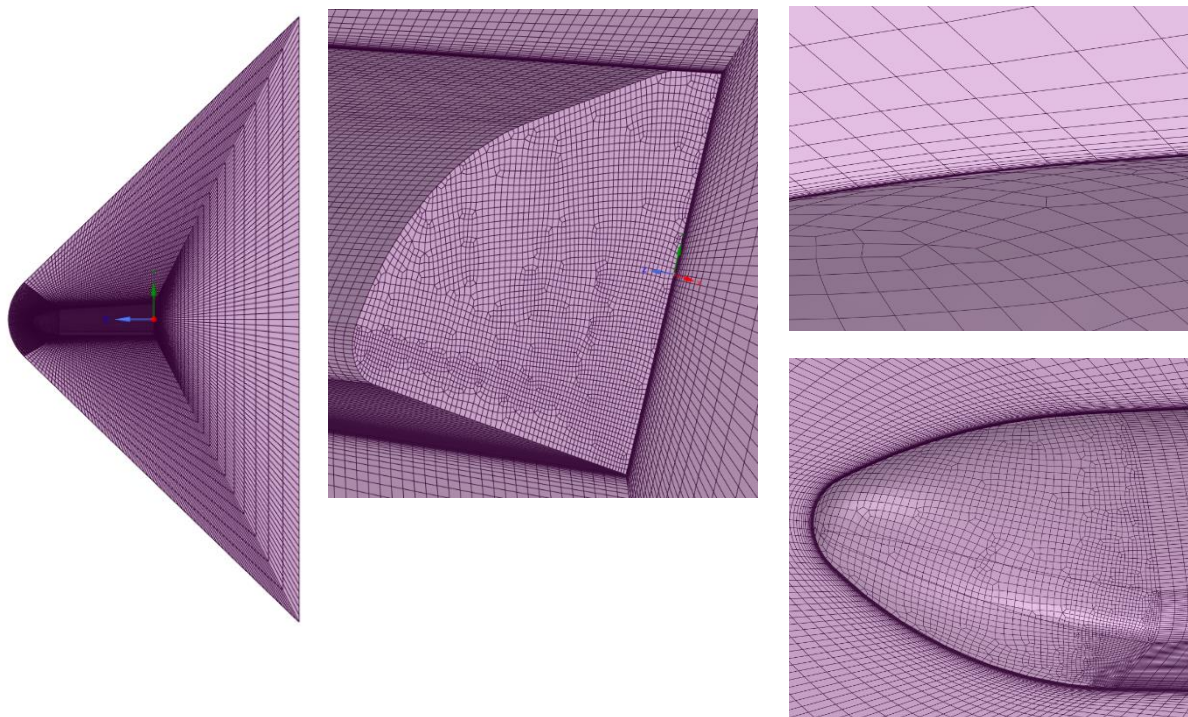
Figure 24: Computational grid for BILBO-3 (representative of all BILBO shapes)

The facets of the lifting body model were grouped as shown in Figure 25Figure to allow for more meaningful and accurate analysis based on surface location. The freestream conditions were set as per Table 1.

Figure 25: Face groups of BILBO shapes

Results and discussion

Force coefficients

Figure 26 demonstrates that L/D ratio is at a maximum with a flat underbelly (increasing by 3.9% between BILBO-1 and BILBO-3 at Ma=16), as expected from supersonic flat plate theory, and decreases approximately exponentially with underbelly radius. Interestingly, the 12m concave shape performed 0.8% better than the 6m convex shape at Ma=16. he results for L/D ratio at α=30° at very close, possibly within the realms of CFD model or simulation error
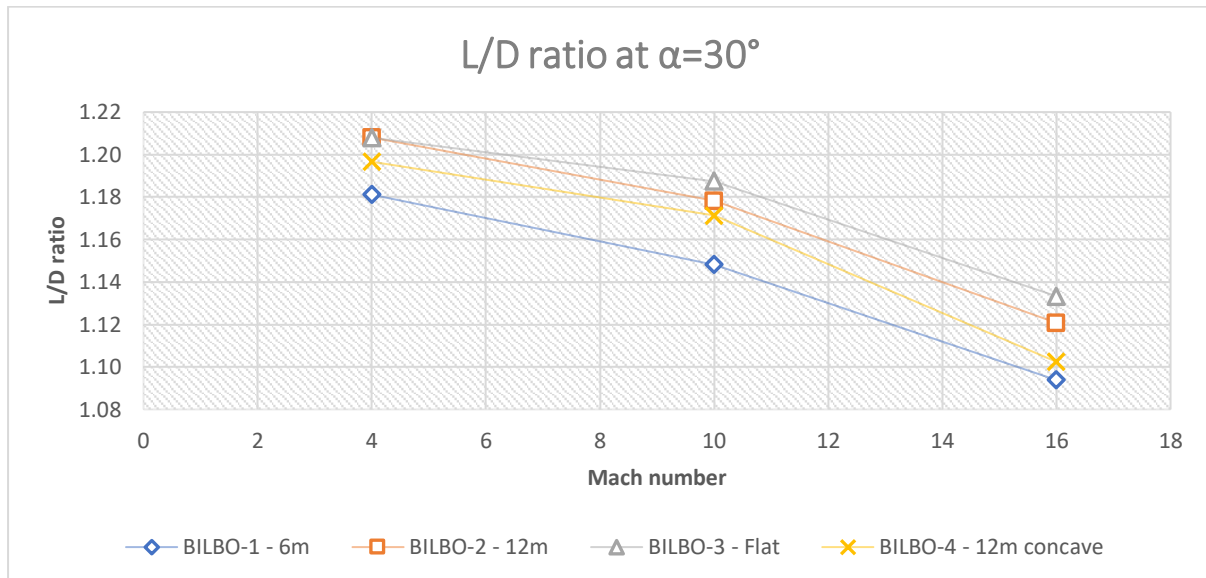
Figure 26: L/D ratio of lifting body shapes at $\pmb{\alpha}$=30°

It might therefore be more effective to repeat these simulations at a lower α of 10° to display a wider range of L/D ratios, similar to that shown in (Dilao & Fonseca, 2015) for the Space Shuttle.
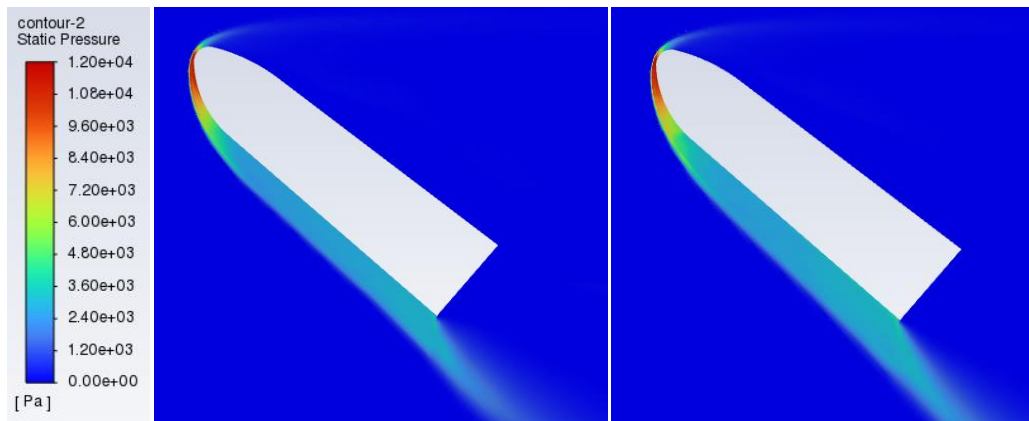
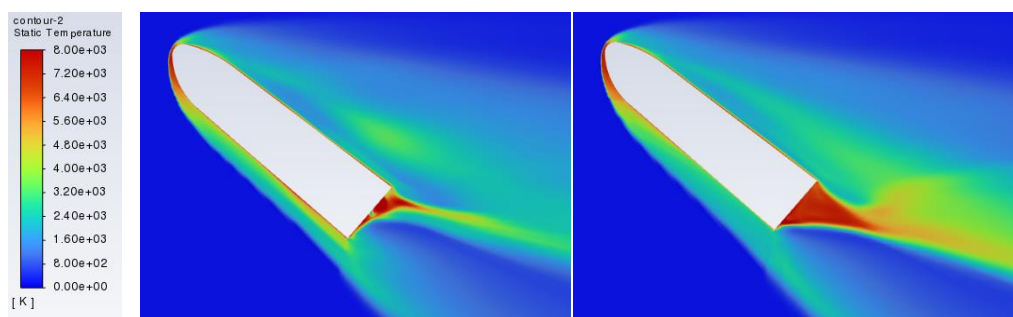**Figure 27:** Static pressure contour of BILBO-1 and BILBO-3 at Ma=10, α=30°

Figure 28: Static temperature contour of BILBO-1 and BILBO-3 at Ma=10, α=30°
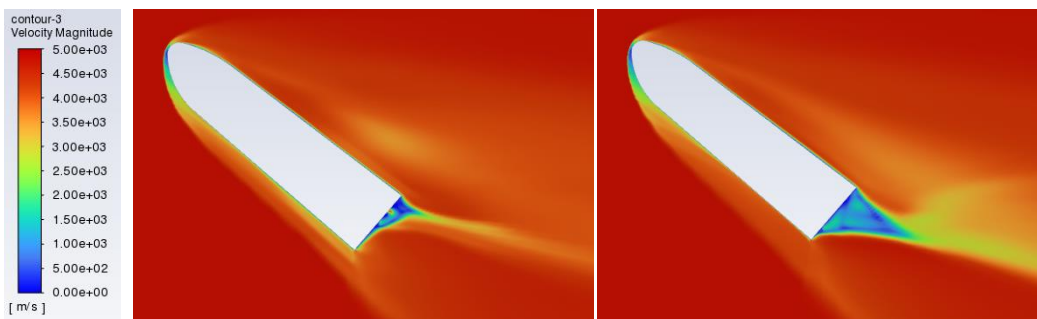

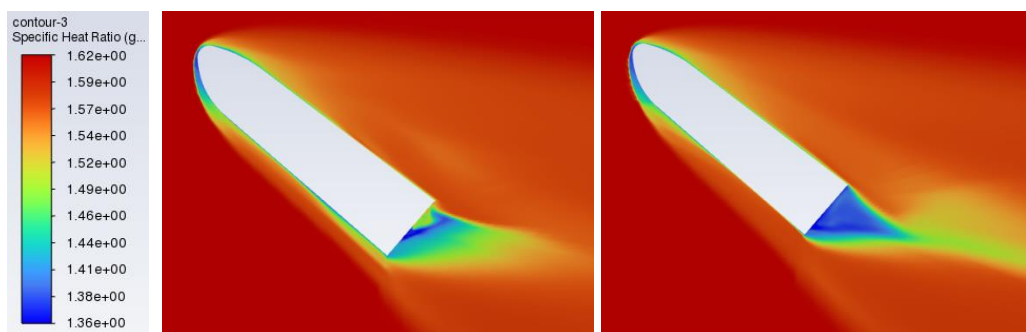**Figure 29:** Velocity magnitude contour of BILBO-1 and BILBO-3 at Ma=10, α=30°

Figure 30: Specific heat ratio contour of BILBO-1 and BILBO-3 at Ma=10, α=30°, demonstrating non-equilibrium flow
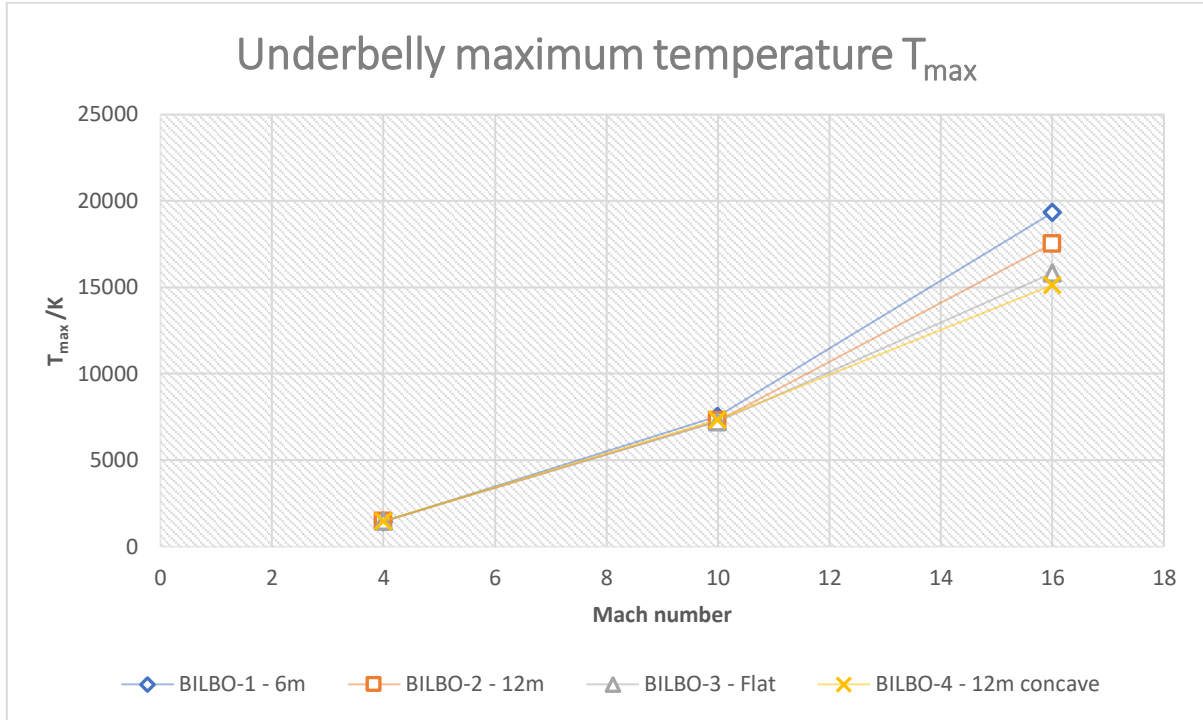
Thermal characteristics

Figure 31: Maximum underbelly temperature plotted against Mach number

Contrary to the original hypothesis, maximum underbelly surface temperatures were found in **Error! Reference source not found.** 31 to increase by 18% between BILBO-3 and BILBO-1. This suggests that the body with a blunter underbelly (BILBO-3) is producing a greater bow shock standoff distance and dissipating more of the heat away from its surface. This is visible in Figure 29.

However, the predicted surface flow temperatures seem unrealistically high, even when using the real gas approximation model – maximum underbelly temperature is ~19000K for Ma=16. For comparison, the Space Shuttle recorded a maximum stagnation temperature of 1921.15K (Chapline & Hale, 2011), and 19000K is significantly higher than the surface temperature of the Sun. However, these temperatures are feasible and within reason for the surrounding flow (Anderson, 1984), suggesting the error lies with the boundary layer simulation.

Using the Sutton-Graves and Boltzmann Law, the theoretical maximum stagnation point temperature for this body and operating conditions is 1715.6K - only 8.4% of the CFD predicted maximum nose T_w of 19898.9K for BILBO-1.

There are a few possible explanations for this – firstly, that the mesh is not significantly refined enough at the wall to capture the boundary layer thermal gradients, thus overpredicting wall adjacent temperature. However, this seems unlikely, as the meshes were all sized for a y^+ of 1, which should be refined enough considering the mesh dependency study validated that the wall-adjacent temperature was mesh-invariant beyond this y^+ (although this MDS was performed for a lower flow velocity).

Secondarily, the Spalart-Allmaras turbulence model might not be sufficiently accurately simulating turbulent mixing and heat dissipation in the boundary layer. Compressibility modifications to the Spalart-Allmaras described in (Kedia, 2006) and investigation using the RANS k-omega SST model with compressibility corrections (Georgiadis, 2013) should be undertaken to improve RANS turbulence modelling. It is not expected that the use of LES or DES turbulence model would make a significant improvement to surface temperature prediction, as they use RANS modelling for smaller length scale turbulence (as would be expected close to the surface (Kianvashrad & Knight, 2021) anyway.

Thirdly, and in the author's opinion, most likely, is that the effects of radiative heat dissipation are not considered for the undertaken simulations. The assumption was made initially that radiative heating would have a negligible effect, based on literature, but it now seems necessary to implement a radiation model to simulate radiative cooling. A suggestion to consider radiation in Fluent would be to use the energy coupled Discrete Ordinates model. Further simulation and verification of this model for hypersonic application is required.

In addition to these suggestions, it is possible that the use of adiabatic wall temperature rather than calculating with a wall-catalysis model is to blame for the exceedingly high surface temperatures – the flow model used assumes a fully catalytic wall surface, which can generate up to 50% higher heat transfer than using a non-catalytic boundary condition (Candler, 2007).

It is unclear why the good agreement shown in the ELECTRE validation case is not reflected in the final simulations. Potentially, the greater angle of attack of the BILBO shape results in greater turbulence, meaning that there is a greater necessity to simulate radiative heat dissipation or compressibility modifications to the RANS turbulence model. Or perhaps, the lower AoA resulted in more steady state laminar heating to the ELECTRE nose, resulting in a more accurate solution.

Underbelly surface analysis
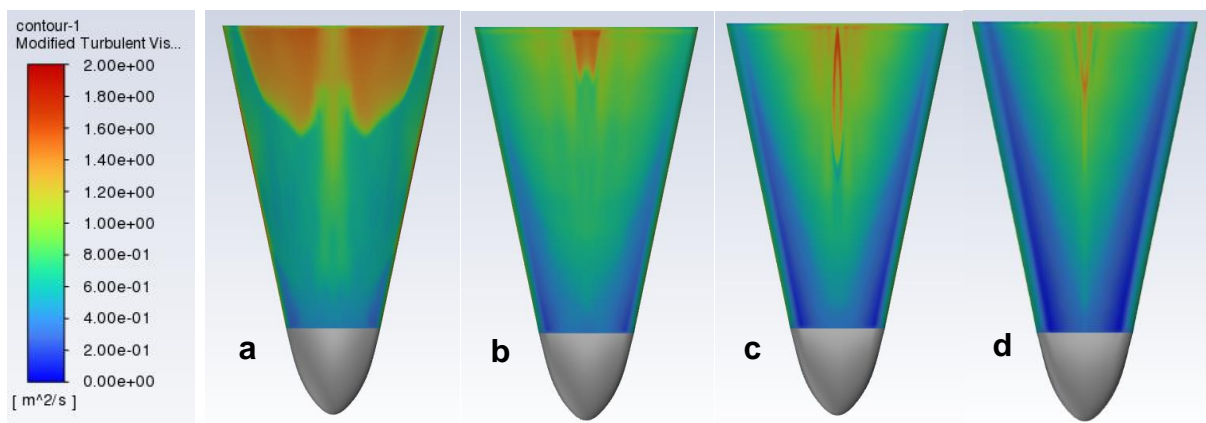
Figure 32: Underbelly turbulent viscosity contour for a) BILBO-1, b) BILBO-2, c) BILBO-3 and d) BILBO-4

The underbelly wall-adjacent temperature contours in Figure 33 show a highly
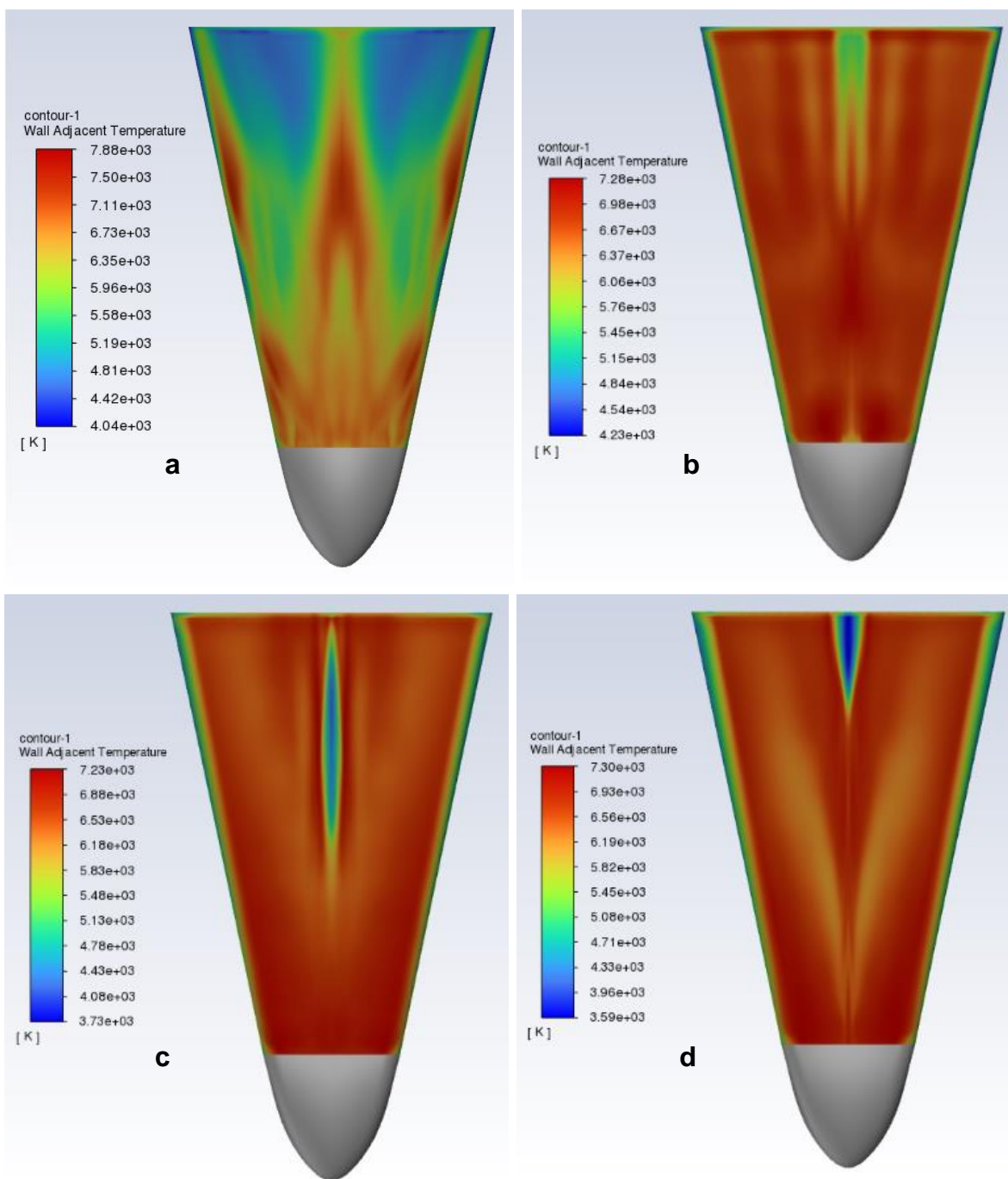
Figure 33: Underbelly wall-adjacent temperature contour for a) BILBO-1, b) BILBO-2, c) BILBO-3 and d) BILBO-4

uneven, turbulent flow region developing on BILBO-1 (6m concave) – this has the potential to make the body unstable, reducing control effectiveness (Coleman & Faruqi, 2009).

Underbelly temperature is distributed relatively evenly across the other three body shape, with only a discontinuity developing along the stagnation line. This could be caused by a lower pressure region developing behind the front of the nose, with mainly sideflow around the nose influencing the rest of the underbelly. This is further reinforced by Figure 34, showing a slow-moving streamline passing over this area of BILBO-3.
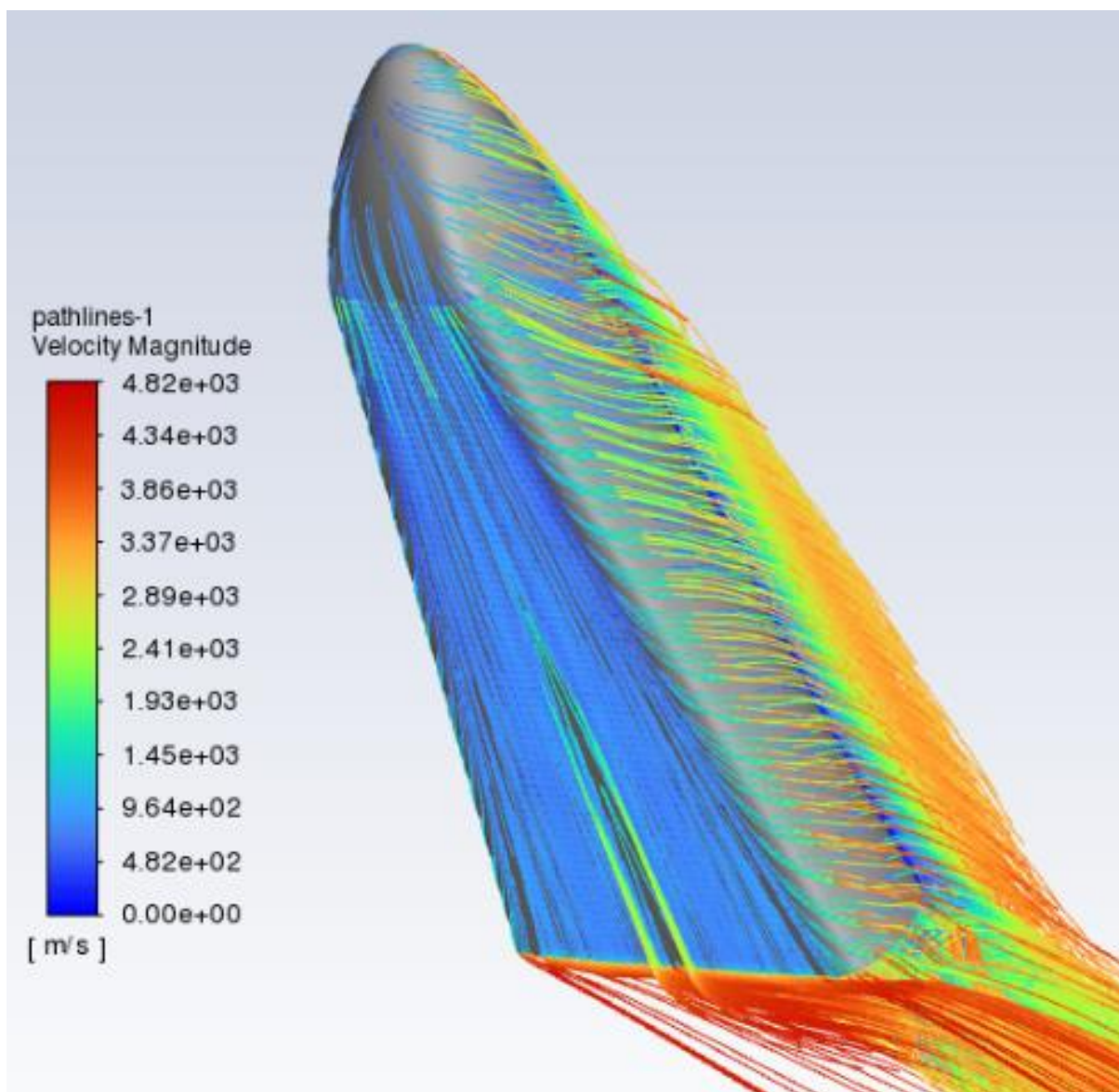

Figure 34: Velocity magnitude pathline of BILBO-3 at Ma=10, α=30°

Figure 35 and Figure 36 show how the bow shock shape is relatively invariant to detailed body geometry, as was suggested initially by (Wan & Liu, 2017). Figure 37 demonstrates the reason why the concave shape has a lower peak temperature – the bow shock standoff distance is greater, allowing the heat to dissipate through turbulent interactions more effectively. However, the turbulent wake region is more pronounced, producing more parasitic drag and reducing L/D ratio. Further optimisation of this body shape could improve this.
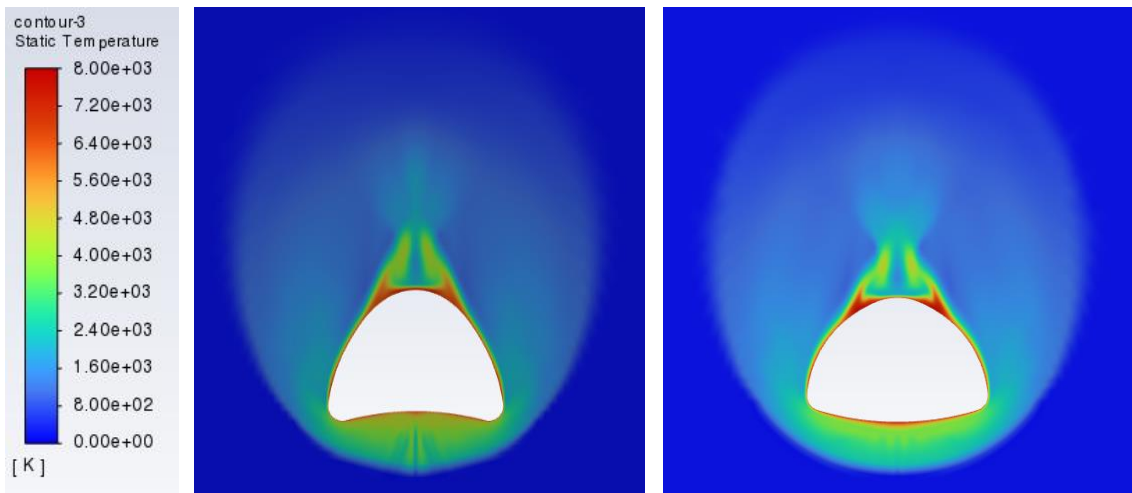

Figure 35: Static temperature contour at x=7m on BILBO-2 and BILBO-4 at Ma=10
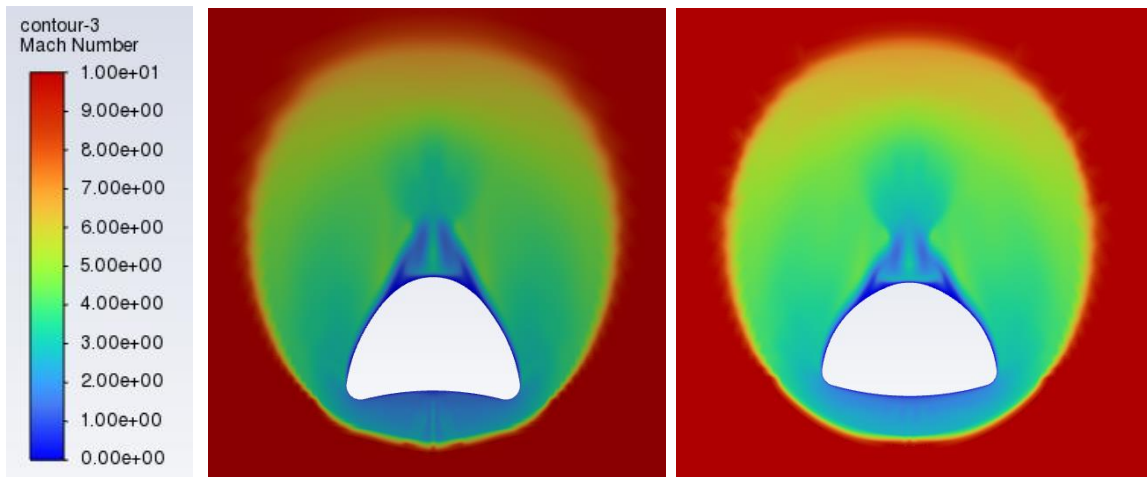
**Figure 36:** Mach number contour at x=7m of BILBO-2 and BILBO-4 at Ma=10

Overall flowfield analysis
It is also clear from Figure 37 that while the mesh was determined to be of sufficient quality to be independent of the output variables of interest, the edges of the clipped 'frontal' shock shape are stair-stepped and rough.
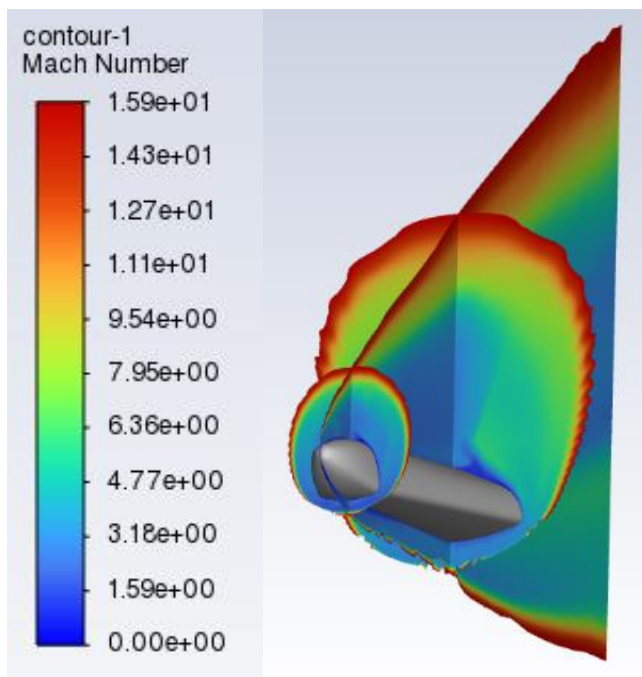
Figure 37: Mach flowfield of BILBO-2 at Ma=16, α=30°

The Mach number flowfield is as expected from theory, with the flow reducing to subsonic behind the stagnation point and in the wake of the vehicle.
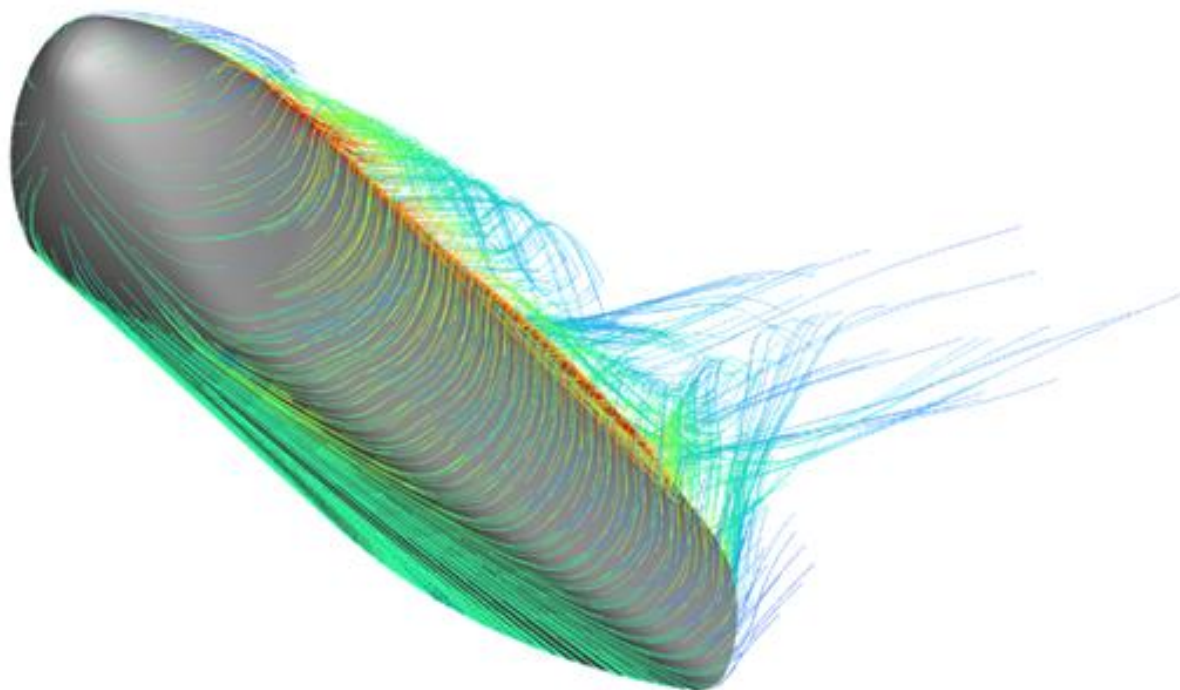
Figure 38: Particle ID pathlines of BILBO-2

Conclusion

Unfortunately, only a semi-successful simulation of re-entry flow has been performed for this investigation, primarily with respect to surface temperature prediction accuracy. Reasonable confidence can be had in the calculated L/D ratios due to their excellent agreement with empirical validation, and the overall flowfield temperatures seem within reason (Viviani & Pezzella, 2015), but the disagreement between stagnation temperatures and theory demonstrates a flaw in the boundary layer or wall simulation methodology.

It was found that increasing underbelly flatness had the effect of improving the L/D ratio by 3.6%. However, maximum surface temperatures were also found to increase with underbelly flatness – this suggests that reducing underbelly radius offers no distinct advantage, either thermally or aerodynamically (in lieu of further analysis with a more accurate flow model).

The experimental 12m concave underbelly was found to offer a 1.6% lower L/D ratio than its convex counterpart, but the peak temperature was predicted to be 13.7% lower at Ma=16 – indeed, it had the lowest T_{max} of all tested body shapes. This offers an intriguing avenue for future lifting body spaceplane designs to minimise aero heating.

This investigation has found that the two-temperature and Park 5-species transport model in Ansys Fluent matches empirical flight heat flux data well, but that wall-adjacent temperature is ~10x greater than could be expected from theory. It should be noted that while there is reason to be suspicious of the absolute predicted surface temperatures, the model still allows for comparison between design choices relative to one another based on surrounding flow temperature.

Recommendations

Further development of this work should focus primarily on implementing a transient LES or DES simulation with coupled Discrete Ordinates radiation model activated, to more accurately refine the prediction of pressure drag and surface temperatures. This is expected to require a larger number of simulations and more computational power.

Additionally, future improvements to this work could include the following:

1. Modification of RANS turbulence models to consider compressibility effects.
2. Implementation of wall-catalysis boundary model.
3. Analysis of more refined, complex lifting body geometry e.g., control surfaces, surface discontinuities etc.
4. Development of a methodology to assess the effect of underbelly radius at subsonic glide velocities and AoA.
5. Aerodynamic investigation of the effect of a body flap on base maximum temperatures.
6. Development of a genetic algorithm or parametric study to automate and optimise lifting body shape design (Skinner & Zare-Behtash, 2018).
7. Analysis of vehicle at lunar or extraplanetary entry velocities (Ma>25) with direct numerical simulation of ionised and highly rarefied flows – 9-species reactions (ionised particles).
8. Further investigation at more values of AoA, Mach and r_u.

9. Further domain size refinement – skewed elliptical domain based on flowfields found in this work.

Nomenclature

Symbol (note italics)	Meaning	Unit
α	Angle of attack	[°]
T_{s_ave}	Area-weighted-average wall-adjacent temperature	[K]
Δ	Change (in results)	[-]
l	Characteristic cell length	[m]
C	Courant number	[-]
y^+	Dimensionless boundary layer quantity	[-]
D	Drag	[N]
C_D	Drag coefficient	[-]
F_D	Drag force	[N]
Δs	First wall cell spacing	[m]
u	Flow velocity	[ms^{-1}]
ρ	Fluid density	[kgm^{-3}]
μ	Fluid dynamic viscosity	[Pa s]
u_∞	Freestream flow velocity	[ms^{-1}]
ρ_∞	Freestream fluid density	[kgm^{-3}]

μ_∞	Freestream fluid dynamic viscosity	[Pa s]
Ma_∞	Freestream Mach number	[-]
p_∞	Freestream pressure	[Pa]
q	Heating flux	[Wm^{-2}]
c_p	Isobaric specific heat	[Jkg^{-1}K^{-1}]
c_v	Isochoric specific heat	[Jkg^{-1}K^{-1}]
E_k	Kinetic energy	[J]
Kn	Knudsen number	[-]
L	Lift	[N]
C_L	Lift coefficient	[-]
F_L	Lift force	[N]
r_u	Longitudinal underbelly radius	[m]
Ma	Mach number	[-]
m	Mass	[kg]
M	Molecular mass	[Da]
p	Pressure	[Pa]
C_p	Pressure coefficient	[-]
q_{rad}	Radiative heat flux	[Wm^{-2}]
γ	Ratio of specific heats	[-]
A	Reference area	[m^2]
Re_x	Reynolds number based on length	[-]
$\dot{R}$	Specific gas constant	[Jkg^{-1}K^{-1}]
q_{stag}	Stagnation point heating flux	[Wm^{-2}]
σ	Stefan-Boltzmann constant	[Wm^{-2}K^{-4}]
S	Sutherland constant	[K]
T_0	Sutherland reference temperature constant	[K]
μ_0	Sutherland reference viscosity constant	[Pa s]
k	Sutton-Graves constant	[-]
T	Temperature	[K]
K	Thermal conductivity	[Wm^{-1}K^{-1}]
ε	Thermal emissivity	[-]
Δt	Time step	[s]
K_t	Time step constant	[-]

L	Vehicle length	[m]
r_n	Vehicle nose radius	[m]
S	Vehicle width	[m]
V	Volume	[m^3]
T_w	Wall temperature	[K]

Abbreviation	Meaning
CFD	Computational Fluid Dynamics
CAD	Computer Aided Design
LEO	Low Earth Orbit
CFX	Ansys CFX
SST	Shear Stress Transport
RANS	Reynolds Averaged Navier-Stokes
AUSM	Advection Upstream Splitting Method
AoA	Angle of Attack
CFL	Courant-Friedrichs-Lewy
NASA	National Aeronautics and Space Administration
TPS	Thermal Protection System
Delta-V	Change in velocity (for rocket engines)
RCS	Reaction Control System
L/D	Lift-to-drag ratio
DDS	Domain dependency study
MDS	Mesh dependency study
SSL	Standard Sea Level
PDE	Partial differential equation
BILBO	Briefly Imagined Lifting Body Orbiter
FMG	FAS Multigrid
LES	Large Eddy Simulation
DES	Detached Eddy Simulation
DNS	Direct Numerical Simulation

References

Anderson, J. D., 1982. *Modern Compressible Flow: With Historical Perspective.* s.l.:s.n.

Anderson, J. D., 1984. *Fundamentals of Aerodynamics.* s.l.:s.n.

Anderson, J. D., 1989. *Hypersonic and High Temperature Gas Dynamics.* s.l.:s.n.

Anderson, J. D., 1992. *Computational Fluid Dynamics: An Introduction.* s.l.:s.n.

ANSYS, 2009. *18.7.1 Overview of FMG Initialization.* [Online]
Available at:
https://www.afs.enea.it/project/neptunius/docs/fluent/html/th/node388.htm

ANSYS, 2009. *26.1 Overview of Using the Solver.* [Online]
Available at:
https://www.afs.enea.it/project/neptunius/docs/fluent/html/ug/node776.htm
[Accessed 2022].

ANSYS, 2009. *6.2.2 Mesh Quality.* [Online]
Available at:
https://www.afs.enea.it/project/neptunius/docs/fluent/html/ug/node167.htm

Balu, R. & Raj, P. L., 2012. *Analysis of Heat Transfer in Hypersonic Flow over Re-entry Configurations,* s.l.: s.n.

Ben-Dor, G., 2007. *Shock Wave Reflection Phenomena.* s.l.:s.n.

Beskok, A., Karniadakis, G. & Aluru, N., 2005. *Microflows and Nanoflows: Fundamentals and Simulation.* s.l.:s.n.

Bhaskaran, R. & Collins, L., 2012. *Introduction to CFD Basics,* s.l.: s.n.

Caminha, G., 2019. *The CFL Condition and How to Choose Your Timestep Size.* [Online]
Available at: https://www.simscale.com/blog/2017/08/cfl-condition/

Candler, G. V., 2007. *Nonequilibrium hypersonic flows & hypersonic nozzle flow modeling,* s.l.: s.n.

Chapline, G. & Hale, W., 2011. *Wings in Orbit: Scientific and Engineering Legacies of the Space Shuttle, 1971-2010.* s.l.:s.n.

Clancy, L., 1975. *Aerodynamics.* s.l.:s.n.

Cockrell Jr, C. E., Huebner, L. D. & Finley, D. B., 1996. *Aerodynamic performance and flow-field characteristics of two waverider-derived hypersonic cruise configurations,* s.l.: NASA.

Coleman, C. C. & Faruqi, F. A., 2009. *On Stability and Control of Hypersonic Vehicles,* s.l.: s.n.

Dilao, R. & Fonseca, J., 2015. *Dynamic Guidance of Gliders in Planetary Atmospheres,* s.l.: s.n.

Ding, F., Liu, J., Shen, C.-b. & Liu, Z., 2017. *An overview of research on waverider design methodology,* s.l.: s.n.

Eberhardt, S., 2009. *Understanding Flight.* s.l.:s.n.

Eckert, E. R., 1971. *Analysis of Heat and Mass Transfer.* s.l.:s.n.

Ferri, A., 1949. *Elements of Aerodynamics of Supersonic Flows.* s.l.:s.n.

Gallais, P., 2007. *Atmospheric Re-Entry Vehicle Mechanics.* s.l.:s.n.

Georgiadis, N. J., 2013. *Recalibration of the Shear Stress Transport Model to Improve Calculation of Shock Separated Flows,* s.l.: s.n.

Gnanasekaran, S., 2017. *Thermal Protection System on Space Shuttle,* s.l.: s.n.

Jain, S., 2007. *Hypersonic nonequilibrium flow simulation over a blunt body using BGK method,* s.l.: s.n.

Josyula, E. & Burt, J., 2011. *Review of Rarefied Gas Effects in Hypersonic Applications,* s.l.: s.n.

Kedia, K. S., 2006. *Effects of Compressibility Correction to Turbulence Models applied to a Hypersonic Re-entry Configuration,* s.l.: s.n.

Kianvashrad, N. & Knight, D., 2021. *Large Eddy Simulation of Hypersonic Turbulent Boundary Layers,* s.l.: s.n.

Ko, W. L., Quinn, R. D. & Gong, L., 1986. *Finite-element reentry heat-transfer analysis of space shuttle Orbiter,* s.l.: s.n.

Kuron, M., 2015. *3 Criteria for Assessing CFD Convergence.* [Online]
Available at: https://www.engineering.com/story/3-criteria-for-assessing-cfd-convergence

Liepmann, H. W., 1957. *Elements of Gas Dynamics.* s.l.:s.n.

Linke, B., Garretson, I., Jan, F. & Hafez, M., 2017. *Integrated Design, Manufacturing and Analysis of Airfoil and Nozzle Shapes in an Undergraduate Course,* s.l.: s.n.

Longo, J. M., 2004. *Modelling of hypersonic flow phenomena,* s.l.: s.n.

Lykoudis, P. S., 1964. *Length of the laminar hypersonic wake during ballistic re-entry,* s.l.: s.n.

Maicke, B. A. & Majdalani, J., 2010. *Evaluation of CFD Codes for Hypersonic Flow Modeling,* s.l.: s.n.

Marvin, J. & Coakley, T., 1989. *Turbulence Modeling for Hypersonic Flows,* s.l.: s.n.

Messiter, A. F., 1963. *Lift of Slender Delta Wings According to Newtonian Theory,* s.l.: s.n.

Miller, C. G., 1998. *Aerothermodynamic Flight Simulation Capabilities for Aerospace Vehicles,* s.l.: s.n.

Mou, S.-C.et al., 2017. *An example for the effect of round-off errors on numerical heat transfer,* s.l.: s.n.

Muylaert, J., Walpot, L. & Hauser, J., 1992. *Standard model testing in the European High Enthalpy Facility F4 and extrapolation to flight,* s.l.: s.n.

NASA Glenn Research Center, 2002. [Online]
Available at: https://www.grc.nasa.gov/www/wind/valid/tutorial/errors.html

NASA Glenn Research Center, 2007. *Normal Shock Wave Equations.* [Online]
Available at: https://www.grc.nasa.gov/www/BGH/normal.html

NASA TFAWS, 2012. *Aerothermodynamics Course,* s.l.: s.n.

Neal Jr., L., 1963. *Aerodynamic characteristics at a mach number of 6.77 of a 9 deg cone configuration, with and without spherical afterbodies, at angles of attack up to 180 deg with various degrees of nose blunting,* s.l.: s.n.

NOAA, 1976. *US Standard Atmosphere,* s.l.: s.n.

Pandolfi, M. & D'Ambrosio, D., 1999. *Numerical Instabilities in Upwind Methods: Analysis and Cures for the "Carbuncle" Phenomenon,* s.l.: s.n.

Papadopoulos, P. et al., 1999. *Current grid-generation strategies and future requirements in hypersonic vehicle design, analysis and testing,* s.l.: s.n.

Park, C., Jaffe, R. L. & Partridge, H., 2001. *Chemical-Kinetic Parameters of Hyperbolic Earth Entry,* s.l.: s.n.

Reed, R. D., 1997. *Wingless Flight: The Lifting Body Story.* s.l.:s.n.

Roy, C. J. & Blottner, F. G., 2006. *Review and assessment of turbulence models for hypersonic flows,* s.l.: s.n.

Shevkar, P., 2016. *What is an acceptable convergence for the Continuity residual in FLUENT?.* [Online]
Available at:
https://www.researchgate.net/post/What_is_a_acceptable_convergence_for_the_Continuity_residual_in_FLUENT/

Sinha, K., 2010. *Computational Fluid Dynamics in Hypersonic Aerothermodynamics,* s.l.: s.n.

Skinner, S. & Zare-Behtash, H., 2018. *State-of-the-art in aerodynamic shape optimisation methods,* s.l.: s.n.

Spalart, P. & Allmaras, S., 1992. *A One-Equation Turbulence Model for Aerodynamic Flows,* s.l.: s.n.

Tong, O., 2013. *Verification and V erification and Validation of the Spalar alidation of the Spalart-Allmar t-Allmaras Turbulence urbulence,* s.l.: s.n.

Ubbelohde, A., 1946. *The Thermal Conductivity of Polyatomic Gases,* s.l.: s.n.

Versteeg, H. K. & Malalasekera, W., 1995. *An Introduction to Computational Fluid Dynamics: The Finite Volume Method.* s.l.:s.n.

Viviani, A. & Pezzella, G., 2015. *Aerodynamic and Aerothermodynamic Analysis of Space Mission Vehicles.* s.l.:s.n.

Wan, T. & Liu, C., 2017. *Drag Reduction Optimization for Hypersonic Blunt Body with Aerospikes,* s.l.: s.n.

White, F. M., 1979. *Fluid Mechanics.* s.l.:s.n.

Wood, R. M., Wilcox Jr, F. J., Bauer, S. X. & Allen, J. M., 2003. *Vortex Flows at Supersonic Speeds.* s.l.:s.n.

Yu, S., Ni, X. & Chen, F., 2021. *CFD Simulation Strategy for Hypersonic Aerodynamic Heating around a Blunt Biconic,* s.l.: s.n.

Appendices are provided separately as supplementary files (see additional downloads for this article).

Yu, S., Ni, X. & Chen, F., 2021. *CFD Simulation Strategy for Hypersonic Aerodynamic Heating around a Blunt Biconic,* s.l.: s.n.